A Modified Method for Estimating Inherent Strains from Detailed Process Simulation for Fast Residual Distortion Prediction of Single-Walled Structures Fabricated by Directed Energy Deposition

Xuan Liang, Lin Cheng, Qian Chen, Qingcheng Yang, and Albert To*

Department of Mechanical Engineering and Materials Science, University of Pittsburgh,

Pennsylvania 15261

*Corresponding author: albertto@pitt.edu

Abstract

Predicting residual distortion in metal additive manufacturing (AM) is important to ensure quality of the fabricated component. The inherent strain method is ideal for this purpose, but has not been well developed for AM parts yet. In this paper, a modified inherent strain model is proposed to estimate the inherent strains from detailed AM process simulation of single line depositions on top of each other. The obtained inherent strains are employed in a layer-by-layer static equilibrium analysis to simulate residual distortion of the AM part efficiently. To validate the model, depositions of a single wall and a rectangular contour wall models with different number of layers deposited by a representative directed energy deposition (DED) process are studied. The proposed model is demonstrated to be accurate by comparing with full-scale detailed process simulation and experimental results. To make the method practical, a small-scale detailed simulation model is proposed to extract the mean inherent strains. Based on this approach, simulation results applied to the rectangular contour wall structures of different heights show that the modified inherent strain method is quite efficient, while the residual distortion of AM parts can be accurately computed within a short time. The improvement of the computational efficiency can be up to 80 times in some specific cases.

Keywords

Residual distortion; modified inherent strain method; process simulation; directed energy deposition; metal additive manufacturing

1. Introduction

Restricted by its subtractive nature, it is difficult to employ machining techniques to produce metal parts with complex geometries, especially those with internal features. However, the demand for complex-shaped parts has increased rapidly since metal parts consisted of microscopic structures (e.g. cellular structures) have been shown to have excellent mechanical performance under certain conditions [1, 2]. Therefore, additive manufacturing (AM) has received much interest lately and is considered an important technique for fabricating complex-shaped workpieces [3]. In modern AM processes, the CAD model of a part is sliced into many thin layers, where each layer is "printed" successively in a bottom-up manner [4-9]. In this way, any complex geometry can be produced by AM. For example, AM has been employed to print complex structures [2, 10] designed by topology optimization [10-15].

The powder bed fusion (PBF) process is currently the most popular AM process for manufacturing complex metal components. For example, selective laser melting (SLM) and electron beam melting (EBM) are powder bed based. The metal part is built in a powder bed via a micro-welding process [16]. On the other hand, directed energy deposition (DED) is more suitable for making

repairs, adding features to an existing component, or even making parts with different materials during the same build. A representative DED process is the LENS (Laser Engineered Net Shaping) [17-19], which is based on feeding powder into the melt pool created by a high energy laser beam. Figure 1 illustrates an example stemming from the use of LENS that will be employed in this work.

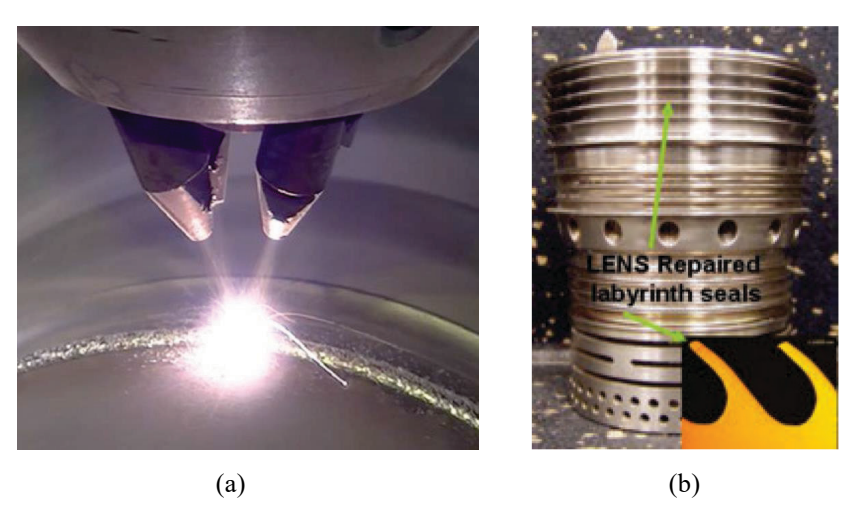


Fig.1 Successful repair case studies using the (a) Optomec LENS system: (b) Inconel 718 compressor seal [18]

At the macroscopic scale, different metal AM processes that employ a high-energy heating source are generally based on similar physical processes involving melting and solidification of metal. Hence in a typical metal AM process, large temperature gradient and high cooling rate occurs due to intensive heat input and large local energy density, which consequently lead to large thermal strains and residual stress or distortion in an AM metal part [20-22].

Unless post stress relief is performed, removal of substrate or support structure after printing would result in further deformation of the AM part and residual stress and strain would redistribute [23]. In order to predict the residual distortion and stress introduced into the part by an AM process, since the physical process of AM has some commonalities with the metal welding phenomenon, some simulation methods focused on the metal welding problem have been extended for metal AM processes [24-28]. Numerical approaches employing the finite element method (FEM) have been implemented [28-32]. Based on the simulations, optimization of laser scanning strategies, build-up directions, or design of support structures could be further investigated [33].

Part scale AM process simulation to compute residual stress and distortion is very time-consuming since it is a long time-scale problem involving transient heat transfer, non-linear mechanical deformation, and addition of large amount of materials [26-28]. Depending on the material under consideration, either a fully coupled or decoupled thermomechanical analysis can be employed. For example, in a decoupled analysis, the thermal analysis is first performed to acquire the temperature distribution at each time step, followed by assigning the obtained thermal load as temperature field at the corresponding step in the mechanical analysis [34, 35]. Obviously, the entire process simulation becomes increasingly time-consuming as large amount of materials are being deposited, and as a result, the size of the modeled part or the number of depositing layers is severely limited. The required simulation time ranges from several hours to days, or even weeks. In order to enable practical AM process simulation, the simulation time must be reduced radically.

Decades ago, the inherent strain method [36-40] was developed and established to enable fast estimation of residual distortion/stress in metal welding. Both simulation and experimental results validate the accuracy and efficiency of the inherent strain method for predicting residual distortion/stress of simple metal welding. Another computationally efficient method inspired by the inherent strain theory is the method of applied plastic strain [41, 42]. It utilizes 2D elastoplastic simulation to calculate the plastic strain and then apply it as an equivalent mechanical load to the 3D model to evaluate residual distortion/stress. Both the inherent strain and applied plastic strain method are capable of significantly reducing the computational cost of the thermomechanical simulation [42, 43]. However, the physical process of AM is much more complicated compared with simple metal welding. Attempts to directly apply the inherent strain or the applied plastic strain method to the AM process have failed to obtain accurate residual distortion or stress of builds with multiple deposition layers. In recent years, some other approaches based on the inherent strain theory have been developed, and the computed inherent strain is imposed onto a macro-scale model to obtain mechanical deformation [44-46]. This method is easy to implement and computationally fast, but it is a challenge to achieve good accuracy in predicting residual distortion at part scale [47].

In this work, a modified method is proposed to estimate the inherent strains accurately from detailed AM process simulation for fast residual distortion simulation of single-walled structures produced by the representative DED process in LENS. These singled-walled structures considered here are composed of laser scan lines deposited on top of each other but not on their sides, except at the connections where two walls join with each other. Obviously, the purpose of considering only these geometrically simple structures is to simplify the problem and model formulation for fast residual distortion prediction. The challenge of doing the same for complex-topological structures is expected to build on top of the model proposed in this work.

The rest of the paper is organized as follows. In Sec. 2, the concept and theory behind the modified inherent strain method will be presented. Section 3 will briefly introduce the thermal and mechanical theory of the detailed simulation for the LENS process to extract the modified inherent strains. In Sec. 4, two numerical examples, together with LENS experimental validation, will be presented to verify the accuracy and efficiency of the proposed method. As a natural extension, Sec. 5 proposes the concept of the mean inherent strain which will be extracted from the two-layer and three-layer line deposition models. Numerical examples will demonstrate that the mean inherent strain can be applied to simple wall depositions containing more layers to accurately predict the residual deformation much faster. Then in Sec. 6, a small-scale simulation model is further proposed to extract the mean inherent strain for applying to different single-walled DED parts and predicting the residual deformation efficiently. Finally in Sec. 7, a few conclusions are drawn and possible future work is discussed.

2. Theory of inherent strain

2.1 Original theory

The original theory of inherent strain is briefly reviewed here based on literature on welding mechanics [38, 48]. In the micro-welding process, the material along the weld path will first be heated, melted, and then solidified in a short time span, which would result in large temperature gradient and complex deformation path. As a result, thermal strain, mechanical strain (both elastic and plastic), and strain due to phase change will be generated and re-equilibrated throughout the

welded part. Since the strain caused by phase change is relatively small compared with the other two kinds of strains, it is usually ignored when computing the inherent strain [34, 35]. (However, if necessary, the inherent strain formulation involving phase change can be accessed as well [49, 50].) After welding is completed, the welded part cools to the ambient temperature.

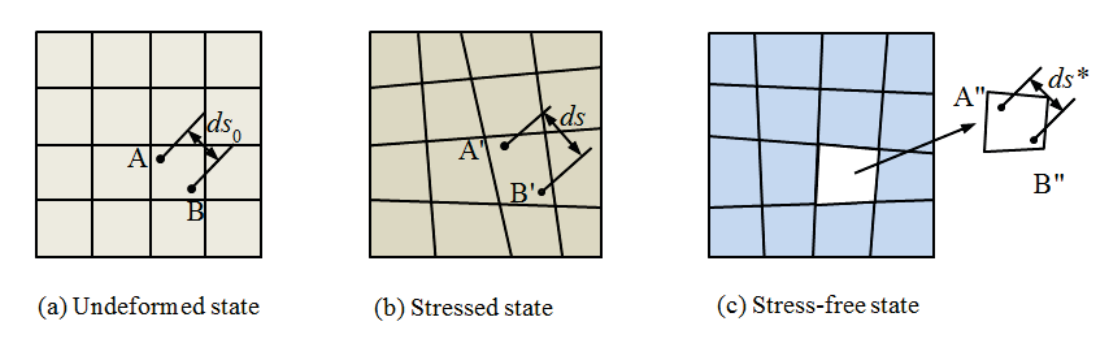


Fig. 2 Original definition of inherent strain for welding mechanics

Now consider two material points A and B in close proximity with each other within a micro-solid as shown in Fig. 2. The distance between the two points is assumed to be ds_0 and ds at the standard and stressed state before and after the welding process, respectively. Then after the residual stress is relieved via relaxation by removing the infinitesimal element containing the two points (see Fig. 2c), the distance between the two points becomes ds^* . By definition, the inherent strain in the element is defined as the residual strain in the stress-relieved state with reference to the undeformed state in Fig. 2(a) before the welding process takes place:

$$\varepsilon^* = (ds^* - ds_0)/ds_0 \tag{1}$$

After the welding process, the metal part is cooled down to the ambient temperature and thermal strain in the part vanishes. Since the reference temperature employed here is always the ambient temperature of the entire system, thermal strain is not concerned and only mechanical strain is involved. Equation (1) can be rearranged as follows:

$$\varepsilon^* = (ds - ds_0)/ds_0 - (ds - ds^*)/ds_0 \tag{2}$$

Given that ds approximates ds_0 under assumption of infinitesimal deformation, Eq. (2) can be further written as:

$$\varepsilon^* = \underbrace{(ds - ds_0)/ds_0}_{\varepsilon} - \underbrace{(ds - ds^*)/ds}_{\varepsilon_e}$$
 (3)

where the first term on the right-hand side is the total mechanical strain ε after the welding is finished, while the second term is the mechanical elastic strain ε_e , which is directly proportional to the stress released.

Practical application of the original inherent strain theory to welding problems makes a key assumption that the elastic strain is insignificant compared to the plastic strain. Hence it follows from Eq. (3) that all the elastic strains vanish and the inherent strain ε^* becomes equal to the plastic strain ε_p generated from the welding process [38-40]:

$$\varepsilon^* = \varepsilon_p \tag{4}$$

From this assumption, components of the inherent strain caused by welding can be determined relatively easily through a relatively small scale welding process simulation of a straight line via FEM, or measured directly from welding experiment. This conventional method applies the inherent strains as the initial strains in the weld regions (i.e. heat affected zone (HAZ) along the welding path [39, 43]) of an elastic finite element model, in order to compute its distortion through a single static analysis. This approach has been shown to be accurate for solving simple welding problems consisted of isolated weld lines [38-40].

For AM problems, the assumption that the elastic inherent strain is insignificant is somewhat invalid and inaccurate for modeling residual stress and distortion in AM parts, because the physical process of AM is quite different from simple metal welding. On the theoretical side, the key assumption that the elastic strain generated by the welding process vanishes is generally not valid for AM parts. During the AM process, new depositions will become mechanically constrained, since new mechanical boundaries continue to emerge with deposition of new tracks and layers. After multiple layers of materials are printed, the mechanical constraints for the previously deposited layers reach a steady state. The elastic strain in the AM process will go into distortion of the remaining AM build. Thus, the inherent strain must contain terms related to elastic strains, in addition to the plastic strain given in Eq. (4) in the original theory.

2.2 Modified theory for additive manufacturing

In order to overcome these issues, a modified inherent strain theory [51] is proposed to estimate the inherent strains from detailed process simulation of an AM part. The physical basis of the proposed modified inherent strain theory is discussed here. Figure 3 schematically illustrates the stress-strain history induced at a material point (black dot), where the heat source passes through and creates a HAZ during an AM process. The starting point of our illustration is when the material point of interest is experiencing the highest temperature due to the heating. For convenience of discussion, assume the material point is both stress free and strain free (Fig. 3A). A large temperature gradient will appear in front of the heat source center [23-25]. As the heat source moves away to the left (Fig. 3B), the material point of interest cools down and solidifies rapidly and experiences a significant amount of shrinkage (compressive strain) but very small compressive stress. The reason is because the yield stress at elevated temperature is very small, and thus the material point of interest yields easily and rapidly, resulting in a large compressive plastic strain. As the heat source moves further away, cooling at the point of interest slows down while the material ahead has just solidified and is undergoing large shrinkage, which induces non-linear tensile stress and strain onto the material point of interest. The tensile stress would reach a maximum point (Fig. 3C). If this were a simple welding problem, the inherent strain can be obtained by relaxing the solid to a stress-free state, and then use the resulting compressive strain as the inherent strain [36, 38]. Different from the simple welding problem, the elastic strain in each deposited layer in an AM process is significantly affected by the evolving mechanical boundaries as additional materials are being deposited. The effect due to the evolving mechanical boundaries on the elastic inherent strain must be accounted for.

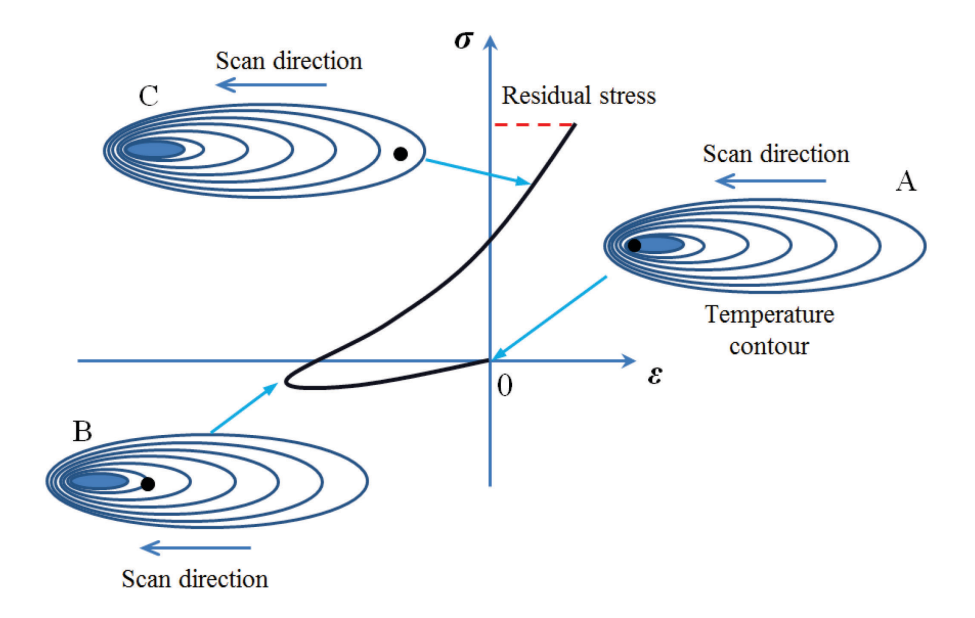


Fig. 3 Schematic illustration of mechanical strain induced at a material point (black dot) during a simple welding process. The heat affected zone (blue ellipse) is generated by the heat source

To simplify the formulation of the modified inherent strain model, consider a simple two-line-layer deposition case in Fig. 4, where one line is deposited on top of a cantilever beam, followed by deposition of another line on top of the first line. For the purpose of computing the inherent strain induced at a material point in the bottom layer, two distinct mechanical states, an intermediate state and a steady state, are defined as follows. The intermediate state is defined as the state when the heat source just passes by and the local (compressive) mechanical strain reaches the largest amplitude (cf. Fig. 4b), whereas the steady state is when the temperature of the whole system cools to the ambient temperature. The modified inherent strain is defined as the difference between the total mechanical strain at the intermediate state and the elastic strain at steady state.

The inherent strain can be expressed mathematically as:

$$\varepsilon^{In} = \varepsilon_{t_1}^{Plastic} + \varepsilon_{t_1}^{Elastic} - \varepsilon_{t_2}^{Elastic} \tag{5}$$

which can also be rearranged as:

$$\varepsilon^{In} = \varepsilon_{t_1}^{Total} - \varepsilon_{t_2}^{Elastic} \tag{6}$$

where t_1 and t_2 denote the time corresponding to the intermediate and steady state for the point of interest in an AM process, respectively. $\varepsilon_{t_1}^{Plastic}$, $\varepsilon_{t_1}^{Elastic}$ and $\varepsilon_{t_1}^{Total}$ represent the plastic, elastic, and total mechanical strain at the intermediate state, respectively, while $\varepsilon_{t_2}^{Elastic}$ represents the elastic strain at the steady state.

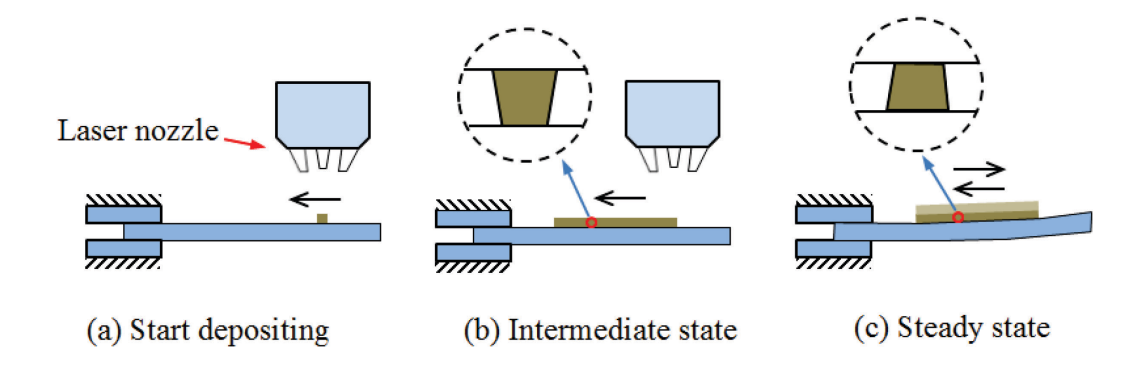


Fig. 4 Two states for the first layer of a two-layer deposition: (a) Depositing starts from the right side; (b) After the first layer is deposited, mechanical boundary for the concerned material points (red circle) is considered as stable; (c) The entire part reaches a steady state at room temperature. Elastic strain is accumulated during cooling and increment of elastic strain between the two states is considered as a result of external work by the surroundings.

Why are these two specific mechanical states chosen? The compressive mechanical strain of a material point at the intermediate state is the direct result of rapid solidification of the melt pool and thus contributes significantly to the inherent strain. The mechanical strain generated up to that state is highly localized and has not spread to its neighboring material yet. What follows is that the material point of interest continues to cool at a much slower rate, and the negative change in thermal strain gradually converts into positive change in elastic strain (i.e. tensile strain), which represents another key contribution to the inherent strain. Note that this change is non-isotropic since it depends on the mechanical boundaries surrounding the point of interest. This is the reason why the elastic strain at steady state is selected for computing the inherent strain.

In the proposed model, only the normal strains are extracted. Indeed, shearing deformation also has some influence on the final residual distortions. However, since the layer thickness is usually much smaller compared with the other two dimensions, the shear stress to the previously deposited lower layers induced by a newly generated upper layer is very limited. As a result, the shearing deformations caused by the thermal shrinkage of the upper layers are neglected in this paper. The results in this work demonstrate that it is acceptable to ignore the shear strains. It will be demonstrated that the model presented above is valid not only for two-line deposition, but for multiple-line deposition on top of each other in the LENS process. Validation of the model will be achieved by comparing with results obtained from detailed process simulation and deformation experiment.

2.3 Assignment of the modified inherent strain

After the modified inherent strains of the elements involved have been obtained through Eq. (6), it is necessary to propose a way to load the strains into the static equilibrium model. In the original inherent strain method, residual deformation of the welded components was estimated by a linear elastic model using the inherent strains as the initial strains. However, it has been demonstrated that the original method of applying inherent strains in a pure elastic analysis cannot obtain a good accuracy when directly applied to the additive manufacturing process. In this work, the modified inherent strains will be employed in a nonlinear elastic-plastic model in the fast method. Since the inherent strains cannot be applied directly as an external load to a finite element model in commercial finite element analysis (FEA) codes, one feasible way is to apply the inherent strains ε^{In} as thermal strains ε^{Th} through the following equations [43]:

$$\varepsilon_i^{Th} = \varepsilon_i^{In}, \ i = x, y, z \tag{7}$$

$$\varepsilon_i^{Th} = \alpha_i \Delta T, j = x, y, z \tag{8}$$

where α_j denotes the equivalent coefficient of thermal expansion (CTE) and ε_i^{Th} represents the equivalent thermal strain in the *j*th direction in the Cartesian coordinate system. ΔT is the temperature change and is taken as unity in our work.

As the modified inherent strains of some elements are compressive and negative, the values assigned for the corresponding CTEs are also negative. Although this may seem unphysical, the resulting deformation obtained from this method is valid. After the CTEs of all the elements in the HAZ are assigned, a unit temperature change is applied to the HAZ as an external load. This is followed by performing a static equilibrium analysis to compute the residual distortion. Since the numerical static analysis is performed just once, the proposed method can save most of the computational time compared with the detailed process simulation.

3. Governing equations of thermomechanical simulation

Since the modified inherent strains have to be extracted based on the history of mechanical strain, we have developed a detailed thermomechanical simulation for the metal AM process, and the key governing equations will be briefly reviewed below. In order to ensure accuracy of the extracted inherent strains, the detailed process model has to satisfy a few characteristics. For example, it should be able to capture the exact peak temperature of any concerned material point in the AM process, since it will influence the mechanical strains of the intermediate state. Therefore, a reasonable heat source model should be employed to capture the shape of the melt pool. Meanwhile, sufficient number of load steps should be used to simulate the detailed laser scanning path. Otherwise, the temperature distribution, especially the far-field temperature, obtained by the thermal analysis may not match the experimental measurement. Moreover, the effects of the evolving mechanical boundaries on the inherent strains extracted cannot be fully considered without enough simulation steps. The number of load steps should be determined based on element size and physical parameters of the heat source such as the laser penetration depth. New elements in each thin layer are activated in each load step to simulate the material depositing process. Some elements are possibly not activated if coarse load steps are employed in the detailed process simulation. To avoid this problem, the number of load steps is first estimated roughly by dividing the deposition layer length by the radius of the laser beam. Then denser load steps have to be employed to ensure that all the elements in a layer will be activated step by step. This is the general rule for considering the least number of load steps are needed to ensure good accuracy for the detailed process model.

3.1 Thermal analysis

Assume a Lagrangian frame Ω and a material point located by $r(r \in \Omega)$ as the reference. Given thermal energy balance at time t, the governing equation can be formulated as follows [35]:

$$\rho C_p \frac{dT(\mathbf{r},t)}{dt} = -\nabla \cdot \mathbf{q}(\mathbf{r},t) + Q(\mathbf{r},t), \mathbf{r} \in \Omega$$
(9)

where ρ denotes the material density; C_p denotes the specific heat capacity; T denotes the temperature field; \mathbf{q} denotes the thermal flux vector and Q denotes the internal heat source. Expression of the thermal flux vector \mathbf{q} can be written as:

$$q = -k\nabla T \tag{10}$$

where k is the thermal conductivity coefficient and ∇T indicates the temperature change. Material properties such as thermal conductivity coefficient and specific heat capacity are usually temperature dependent.

The internal heat source Q exerts a significant influence on the thermal modeling of the AM process, since the heat input is the fundamental cause of the residual distortion and stress. Different mathematical models have been proposed in the literature [50, 52-54] to construct equations of the heat source. The difference between those models is generally different number of degrees of freedom. Among the heat source models, the double ellipsoidal model [55] has been widely used [32, 34, 49, 56, 57], which may be the most sophisticated model proposed so far. The pattern of the heat generation rate is assumed to be Gaussian. However, those equations are generally proposed under a specific condition and should be modified to match the actual size of the melt pool. Acceptable ways for comparing parameter fitting of the heat source model in order to match the geometry in the micrograph can be found in the references [56, 57].

For the thermal analysis, the initial condition regarding the temperature is assigned as follows:

$$T(\mathbf{r},0) = T_0(\mathbf{r},0), \mathbf{r} \in \Omega \tag{11}$$

Equations corresponding to different types of thermal boundary conditions in the AM process are generally classified into three categories:

$$T = \bar{T}, \ \boldsymbol{r} \in \Gamma_D^T \tag{12}$$

$$-k\nabla T \cdot \boldsymbol{n} = \overline{q}, \ \boldsymbol{r} \in \Gamma_N^T \tag{13}$$

$$-k\nabla T \cdot \boldsymbol{n} = h(T - T_a), \boldsymbol{r} \in \Gamma_R^T$$
(14)

Equation (12) gives the Dirichlet boundary condition on the boundary Γ_D^T where the temperature field is prescribed as \overline{T} . Equation (13) gives the Neumann boundary condition on the boundary Γ_N^T , whereas the heat flux is defined with the normal vector \boldsymbol{n} to Γ_N^T ; Equation (14) shows the Robin boundary condition where the surface heat convection with the convection coefficient h between the ambient temperature T_a and the surface temperature T is applied on Γ_R^T . There is no overlap among Γ_D^T , Γ_N^T and Γ_R^T and $\Gamma_D^T \cup \Gamma_N^T \cup \Gamma_R^T = \partial \Omega^T$.

3.2 Mechanical analysis

Quasi-static mechanical analysis is generally implemented to calculate the mechanical response such as the residual distortion and stress for AM builds. The temperature history obtained by the abovementioned thermal analysis is applied to the model as an external load and boundary constraint. The governing equation corresponding to the quasi-static mechanical analysis can be written as follows:

$$\nabla \cdot \boldsymbol{\sigma} + \boldsymbol{b} = \mathbf{0}, \boldsymbol{r} \in \Omega \tag{15}$$

where σ denotes the stress tensor and \boldsymbol{b} represents the body force vector of the model. As for the boundary conditions, the Dirichlet and Neumann boundary conditions will be taken into account, as formulated in Eqs. (16) and (17) as follows:

$$\boldsymbol{u} = \overline{\boldsymbol{u}}, \boldsymbol{r} \in \Gamma_D^M \tag{16}$$

$$\boldsymbol{\sigma} \cdot \boldsymbol{n} = \bar{\boldsymbol{t}}, \boldsymbol{r} \in \Gamma_N^M \tag{17}$$

where \boldsymbol{u} denotes the displacement vector and is prescribed $\overline{\boldsymbol{u}}$ on the mechanical boundary Γ_D^M . In Eq. (17), dot product of the stress tensor $\boldsymbol{\sigma}$ and normal vector \boldsymbol{n} is the surface traction vector, which is prescribed $\overline{\boldsymbol{t}}$ on the mechanical boundary Γ_N^M .

In this work, the temperature dependent elastic-plastic material model is utilized. The constitutive equation of the material model can be written as follows:

$$\sigma_{ij} = C_{ijkl}(E_{kl} - E_{kl}^p - E_{kl}^{th}) \tag{18}$$

where C_{ijkl} denotes the fourth-order tensor of elasticity; E_{kl} , E_{kl}^p , and E_{kl}^{th} represent the total, plastic and thermal strain, respectively. The associate J_2 plasticity model with temperature-dependent mechanical properties is used in the analysis. The details of the process model can be found in Ref. [56].

3.3 Element activation method

In an AM process, materials are deposited in a layer-by-layer manner. The elements in each of the deposited layers do not have any contribution to our FEA until the heat source arrives. As the heat source moves sufficiently close, the elements surrounding the laser spot will be deposited. When the deposition ends, all the elements involved in the deposition are activated and contribute to the thermal and mechanical analysis. For this purpose, the birth and death element activation method is utilized in this work [34, 56, 58].

Advantages of the birth and death element technique include the following two aspects. On the one hand, no ill-conditioning problem will be introduced to the matrix of structural global stiffness and mass. On the other hand, only the degrees of freedom of active elements are involved, which contributes to a relatively small algebraic system to solve. Nevertheless, the birth and death element technique has the following disadvantages. First, it is not easy to implement the method into the commercial FEA software through user-defined subroutines. Second, renumbering of the equations and re-initialization of the solver are performed every time new elements are activated, which will negate savings of the computational cost.

In addition, an element activation criterion is required to determine whether an element needs to be activated in the simulation. A feasible activation criterion combined with the double ellipsoid heat source model is employed in this paper. The inactive elements are activated where the heat power is higher than 5% of the maximum value at the ellipsoid center [56].

3.4 Validation experiment

The LENS 450 metal AM system (Optomec, Albuquerque, NM) used to perform our experiment is shown in Fig. 5, and the material being printed is a titanium alloy called Ti-6Al-4V (Ti64). A

fixture that mounts onto the build platform is designed to hold a small substrate for deposition, which acts as a cantilever that allows residual deformation to be measured (see Fig. 6(a)). The LENS system allows the input of the exact build path and process parameters such as the laser power, scanning velocity, and powder feed rate.

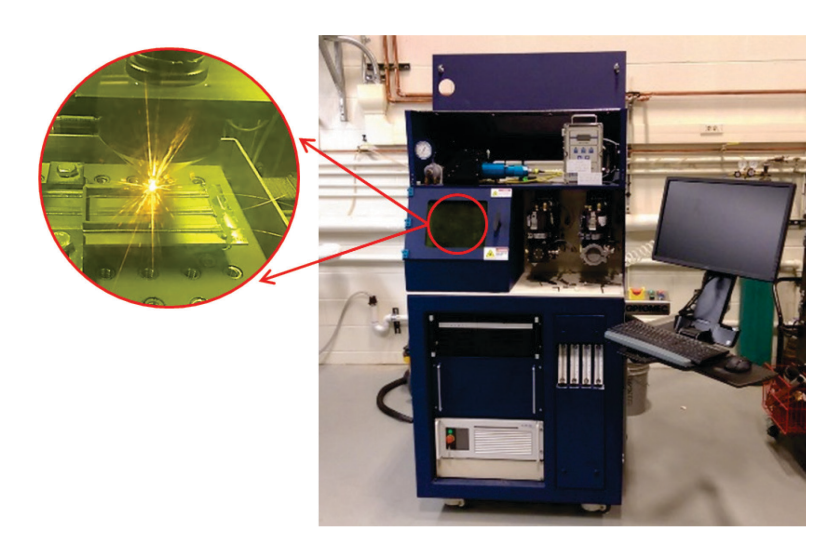


Fig. 5 The Optomec LENS 450 metal printer

After printing is completed, a 3D laser scanning device (FARO arm) shown in Fig. 6(b) is utilized to measure the residual distortion of the part in the vertical direction. Before measuring the residual distortion, a calibration test against the laser scanning device should be performed first. Difference between two scanned configurations of an identical part is taken as the system error of the measurement. It suggests that the measurement error of our 3D laser scanning device is ± 0.075 mm. This resolution is good enough for our experimental measurement.

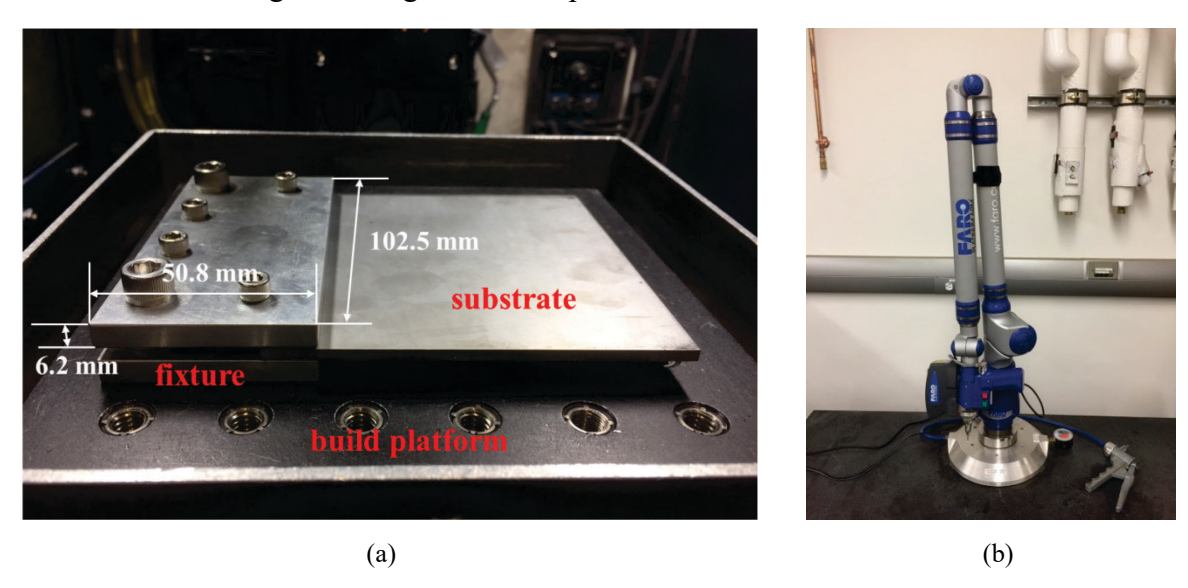


Fig. 6 Illustration of the experimental setup (a) the fixture and substrate (b) the 3D laser scanning device

Before the fixture and substrate are mounted onto the build platform in the chamber of the LENS machine, the bottom surface of the undeformed substrate is scanned as a reference. After a metal part has been deposited onto the substrate, the bottom surface of the deformed substrate is scanned for a second time to compare with the reference. As a result, the displacement could be obtained and plotted easily. Accuracy of our detailed LENS process model of Ti64 has been validated in this manner in our previous work [56], in which all the specific material parameters, heat source parameters, and boundary conditions can be found. Hence only a few details about the detailed process model will be provided below, and interested reader is referred to Ref. [56] for further details.

4. Validation of modified inherent strain theory based on full-scale process simulations

In this section, two examples will be employed to validate the modified inherent strain model proposed in Eq. (6). All the process modeling, computational, and post-processing tasks were coded using the APDL environment in the commercial ANSYS simulation software. The classical mechanical package in ANSYS r17.2 was called to read the input files and conduct the thermal and mechanical analysis. The element type used was the solid brick element containing 8 nodes named solid185. Each node has three degrees of freedom corresponding to the displacements (UX, UY, UZ). This element type has good bending behavior even when the mesh is coarse and is one of the most commonly used element type. Results with excellent accuracy can typically be obtained using this element type.

In the following two examples, there is one element in the thickness dimension of a single layer, and the thickness of the element is close to the laser penetration depth. The number of elements in the entire deposition thickness equals the number of physical layers. This element size in the thermomechanical simulation was shown to have good accuracy compared to our experiments where the thermal history and residual deformation were measured. Based on past literature and our own experience, it is a common practice to employ only one element in the layer thickness in many references [26, 27, 34, 35, 56]. It is clear that finer mesh with two or more elements in the thickness can also be used for the simplified detailed process model. However, it will be very expensive to implement the simulation.

4.1 Single wall deposition model

The first example employed to validate the modified inherent strain model proposed is a single wall produced by depositing multiple single tracks on top of each other on a substrate. The model and a back-and-forth laser scanning path are shown in Fig. 7. The left end of the substrate consists of two fixtures connected to the platform in the chamber of the LENS machine. Geometrical parameters including the length, width and height of the line depositions are shown in Table 1 below. The size of the substrate is $102 \times 102 \times 3.22$ mm³. Both the deposition and substrate are made of Ti64.

Number of layers	Length /mm	Width /mm	Height /mm
1	44.57	2.0	0.99
2	44.57	2.0	1.80
3	44.57	2.0	2.70
5	44.57	2.7	4.75
10	36.00	3.0	9.00

Table 1 Geometrical parameters of the LENS deposits

For the deposition, the process parameters employed are as follows: Laser power of 300W, scan velocity of 2.0 mm/s, and powder feed rate of 8 rotations per minute (RPM). The input heat source model employs the double ellipsoid model in which the absorption efficiency is taken to be 45% [34, 56]. The laser scanning starts from a designate point close to the free end of the substrate and moves toward the clamped end. When printing the next layer, the laser beam scans in the opposite direction, i.e., from the clamped side to the free end. The laser scanning strategy repeats itself every two layers. Material property of Ti64 is temperature dependent and detailed information can be found in Refs. [29, 56]. The total processing time is 1,600 seconds with the entire heating and cooling process included. Without specific instructions, residual distortion in all the figures is in unit of meter.

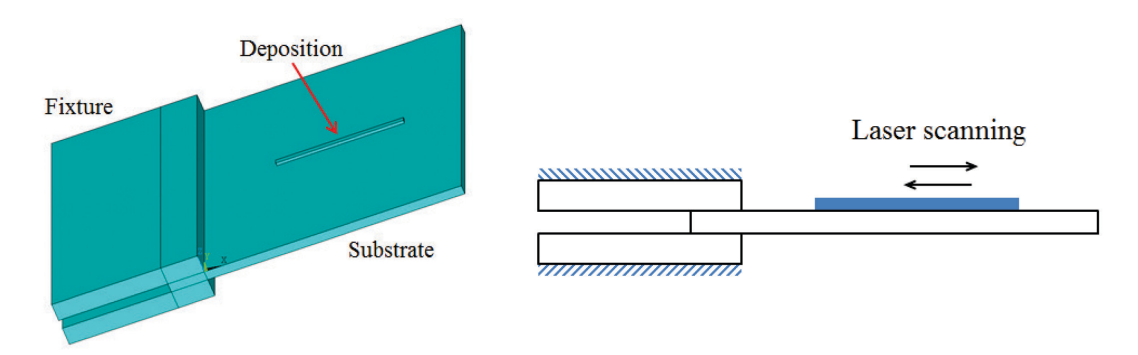


Fig. 7 A line deposition and the laser scanning path

It could take a few hours to finish running the detailed process simulation. Usually the maximum residual distortion and stress are of the most concern. As shown in Fig. 8, the displacement profile of the one-layer line deposition in the vertical direction is obtained by the detailed process simulation. The maximum distortion occurs at the free end of the substrate and the value is 0.326 mm. In addition, many elements in the deposition are at yield state and their von Mises stress is \sim 765 MPa, which agrees with the yield criterion with respect to the mechanical plastic property of Ti64 at room temperature.

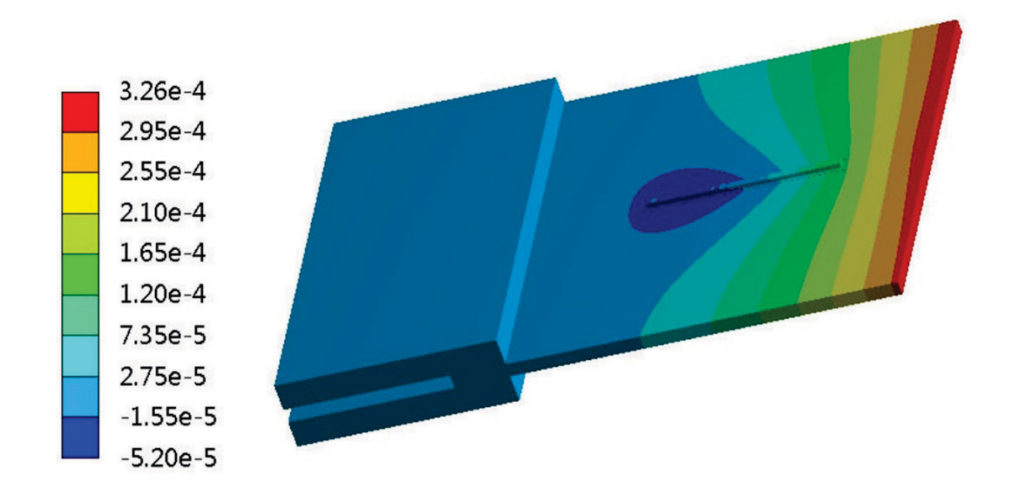


Fig. 8 Vertical residual distortion (unit: m) of a one-layer line deposition by detailed process simulation

Before extracting the inherent strains, it is necessary to show how the HAZ should be estimated from the detailed process simulation. The plastically deformed areas indicate the existence of the inherent strains. Besides the metal depositions, an extension has to be considered since the plastic deformations are also found in the local areas of the substrate. A thin layer beneath the metal deposition is deformed due to the high temperature caused by the intensive heat input when the first layer of the metal part is built. To determine the reasonable HAZ, the simplest way is to investigate the distribution of the residual plastic deformations after the entire deposition is finished in the detailed simulation. All the plastic deformed elements are selected according to the range of their coordinates. Then the inherent strains of those selected elements are calculated based on the simulation results.

In order to illustrate that the conventional theory of inherent strain is not valid for AM, the inherent strain is computed based on Eq. (4) and then is utilized to compute residual distortion. Only the final state at room temperature is concerned according to the definition of conventional inherent strain model. Both single-layer and multi-layer depositions were investigated. Computed results of the vertical residual distortion are listed in Table 2 and compared with those obtained by detailed process simulation. The computational times of the two different methods are also shown to demonstrate the advantage of the inherent strain method as a fast prediction tool. The large errors shown in the table suggest that the conventional inherent strain theory is not accurate for estimating the residual distortion of an AM process. Therefore, the modified theory is proposed in this work.

Table 2 Maximum vertical residual distortion of the part after LENS deposition of a straight line and computational times by detailed process simulation and conventional inherent strain method

Number Detailed process simulation		Conventional i	_ Distortion		
of layers	Distortion (mm)	Computational time (min)	Distortion (mm)	Computational time (min)	error (%)
1	0.326	21.6	0.170	1.2	47.9
2	0.502	33.0	0.299	1.8	40.4
3	0.584	43.7	0.412	2.2	29.8
5	0.937	57.6	0.672	3.2	28.3
10	0.663	114.4	0.478	4.2	27.9

In order to illustrate how to evaluate the inherent strains using the modified theory based on the detailed process simulation, the two-layer line deposition case is taken as an example, and the inherent strains of the elements in the lower layer are concerned. The critical step here is to determine the reasonable time steps corresponding to the intermediate and steady states. Since the length of the line deposition is relatively small, an easy way to determine the intermediate state (when the compressive plastic strain reaches the maximum) to be the time step for the concerned layer when the deposition of the next upper layer is just completed. This time step is thus employed as the intermediate state for the elements in the concerned layer to extract the total mechanical strains. After the entire printing process is complete, the deposition reaches the steady state and then the elastic strains of the elements in the lower layer are extracted. Using Eq. (6), the modified inherent strains in three dimensions can be calculated. The averaged inherent strain values against the normalized deposition length are plotted in Fig. 9. The longitudinal direction represents the major laser scanning path, while the transverse direction is perpendicular to the in-plane scanning direction. The vertical direction indicates the build direction. Using the same method, the inherent strains of the elements in all the deposition layers can be obtained from post-processing of the detailed process simulation results. Figure 9 shows a general distribution pattern of the inherent strains in the AM metal parts, but the magnitudes of the inherent strains in different layers may be a little different due to the variation of the laser scanning paths.

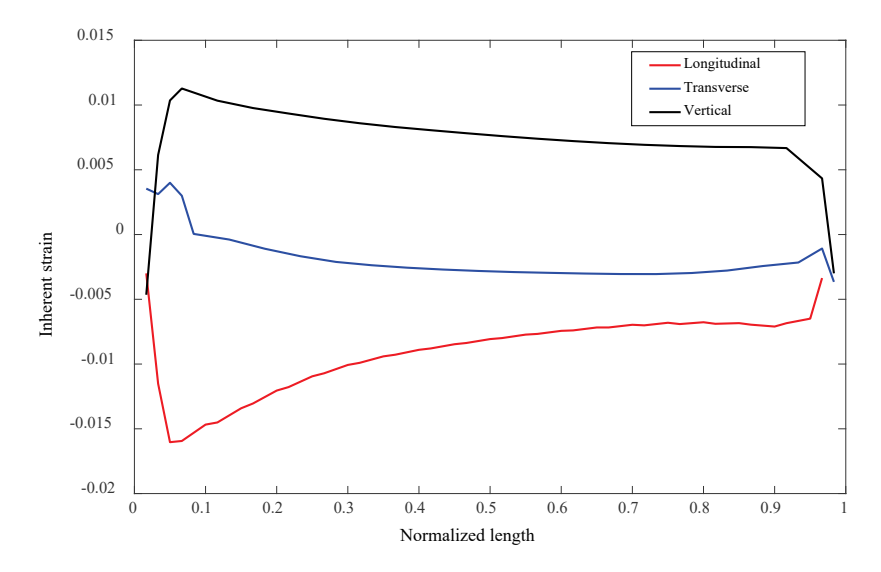


Fig. 9 The extracted elemental inherent strains of the lower layer in a two-layer line deposition

After the inherent strains are obtained using the modified theory, residual distortion can be computed through a single static equilibrium analysis within a few minutes on a desktop computer. Note the conceptual formulation of the modified inherent strain method is illustrated using the two-pass deposition (see Fig. 4) because it is more straightforward to explain the intermediate state for a typical material point in the metal depositions. However, it does not mean the proposed method is not applicable to the single track experiment. The same concept of finding the rapid solidification state still needs to be applied to the one layer case to extract the inherent strains. For the one-layer line deposition, the distribution pattern of the vertical residual distortion of the part, as shown in Fig. 10, is almost identical to that shown in Fig. 8, and the maximum vertical distortion is 0.348 mm. Excellent agreement can been observed between the results computed by the detailed process simulation and the modified inherent strain method.

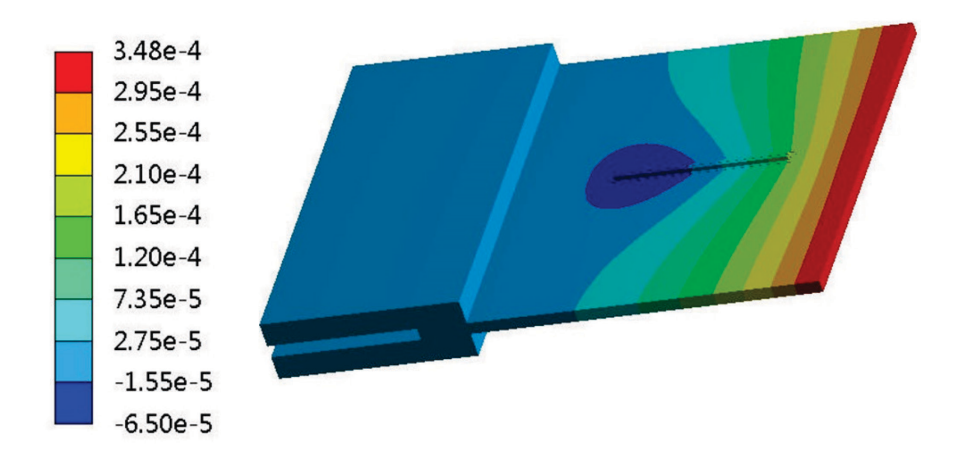


Fig. 10 Vertical residual distortion (unit: m) of the one-layer line deposition by modified inherent strain method Moreover, vertical residual distortions resulting from line depositions for different layers obtained

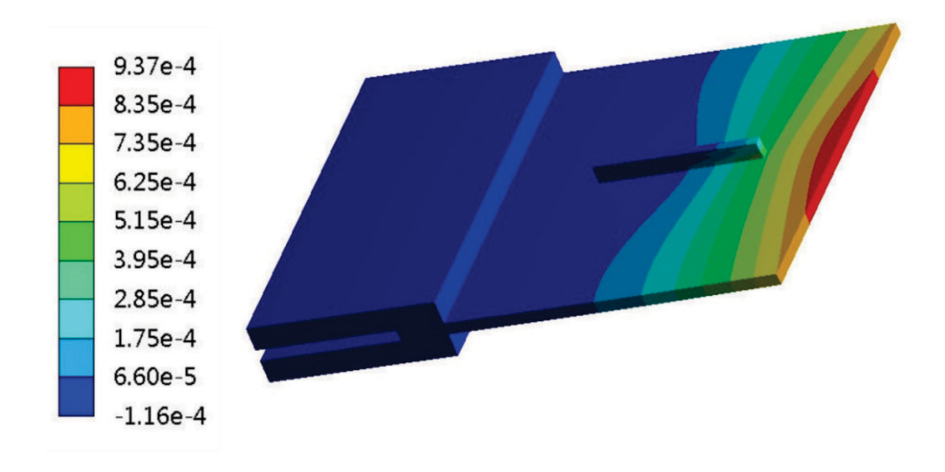
by detailed process simulation and the modified inherent strain method are compared in Table 3.

Note that the errors in the vertical displacement computed by the modified theory are 5~15 times smaller than the corresponding ones obtained by the original theory when compared to the detailed process simulation results. Since there is no obvious trend in the errors for different number of layers (Table 3), the assumption that the mechanical boundary condition reaches steady state after one layer has been deposited seems to be valid. This makes extracting the inherent strains from detailed process simulation much more straightforward. Whereas, Table 3 contains result for the two-layer line deposition, and the prediction error of 10.9% is the largest among all the different cases. Although the conceptual formulation of the modified inherent strain theory is illustrated using a two-layer deposition, it is not expected to represent the best result for the two-layer case. Since even the largest percentage error is of the same magnitude to the ten-layer case (8.4%) in Table 3, this discrepancy is insignificant. Thus, the relative large error in the case of the 2-layer model is believed to be a random occurrence

Table 3 Maximum vertical residual distortion of the part with line depositions and computational times by detailed process simulation and modified inherent strain theory

Number of	Detailed p	Detailed process simulation		Modified inherent strain method		
layers	Distortion (mm)	Computational time (min)	Distortion (mm)	Computational time (min)	_ Distortion Error (%)	
1	0.326	21.6	0.348	1.5	6.7	
2	0.502	33.0	0.557	2.1	10.9	
3	0.584	43.7	0.606	2.6	3.8	
5	0.937	57.6	0.956	3.5	2.0	
10	0.663	114.4	0.607	4.4	8.4	

Next, the vertical residual distortion profiles of a five-layer line deposition obtained by detailed process simulation and modified inherent strain method are shown in Fig. 11(a) and 11(b), respectively. The distribution of the vertical distortion is symmetric in the plane since the laser scanning path and the mechanical boundary conditions are both symmetric in this problem. Very good agreement is observed by comparing the two figures. Both the accuracy and efficiency of the proposed method are further validated.



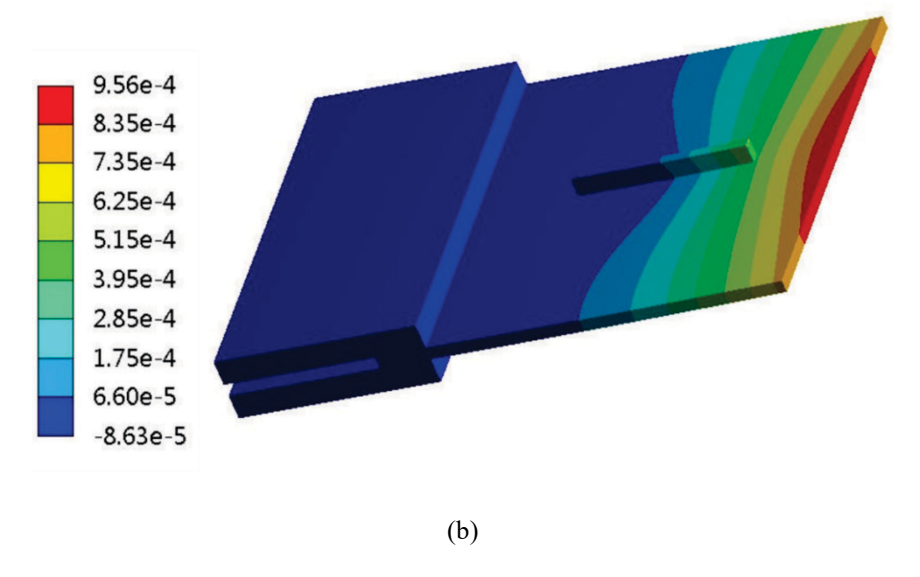


Fig. 11 Vertical residual distortion (unit: m) of the five-layer line deposition by (a) the detailed process simulation (b) the modified inherent strain method

In terms of computational efficiency, the computational times of the detailed process simulation and the modified inherent strain method are also shown in Table 3. Generally, a ~20x speedup can be achieved using the modified inherent strain method as compared with detailed process simulation. Especially for the depositions containing more layers, the computational efficiency becomes higher, see the 10-layer case in Table 3. Clearly, with more development, the proposed method has great potential in fast prediction of residual deformation in an AM part.

4.2 Rectangular contour wall deposition model

In order to further demonstrate accuracy of the proposed method, the rectangular contour wall deposition shown in Fig. 12 is investigated here. In the printing process, the laser scanning path is counterclockwise as illustrated by arrows in the figure. Each side of the model can be considered as an independent single-walled deposition, since the intersection of any two neighboring sides is relatively small. Since an intermediate state containing a stable mechanical boundary is critical in the proposed theory, the intermediate state of the elements in the layer of interest is defined as the moment when the overlaid layer on the same side has just been deposited.

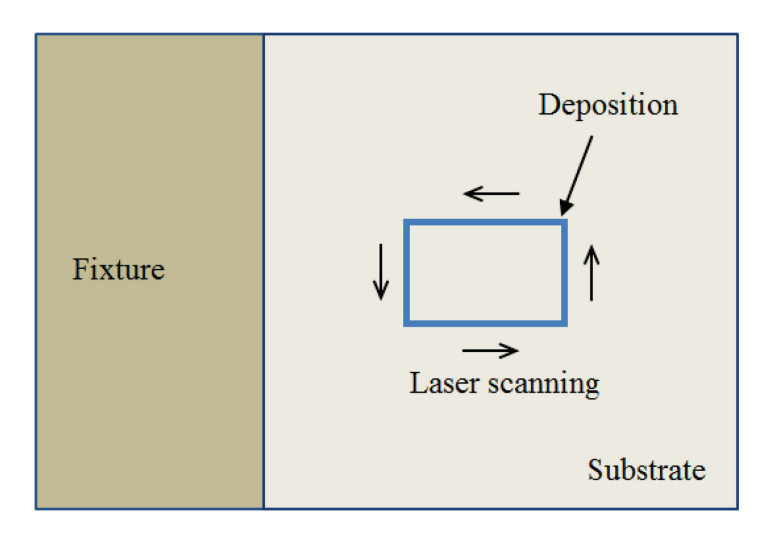


Fig. 12 Laser scanning path of the rectangular contour deposition

First, we conduct detailed process simulation of the rectangular contour wall with different number of layers. In particular, for the five-layer rectangular contour wall, dimension of the substrate is set to 101.6×101.6×3.18 mm³ in order to be consistent with the experimental setup. For other cases, the size of the substrate is the same as in the first example. Geometrical parameters such as the length (L), width (W), thickness (T) and height (H) of the rectangular contour depositions are shown in Fig. 13 and also listed in Table 4 below. The process parameters employed are as follows: Laser power 300W, scan velocity 2.0 mm/s, and powder feed rate of 6 RPM. In addition, to ensure numerical convergence of the detailed process simulation for the five-layer contour, the substrate is meshed using two layers of elements in the thickness direction, while three layers of elements are employed for the other cases. To ensure the choice does not create an unfair comparison, the influence of the element mesh to the numerical simulations has been investigated through a series of process simulations. For the five-layer contour deposition case, two cases were investigated where the substrate was meshed into one and two elements in the dimension of thickness, respectively. It is found that the influence by the element mesh of the substrate to the entire residual distortions is negligible, which indicates that the substrate mesh is not a concern to the validation of the proposed method.

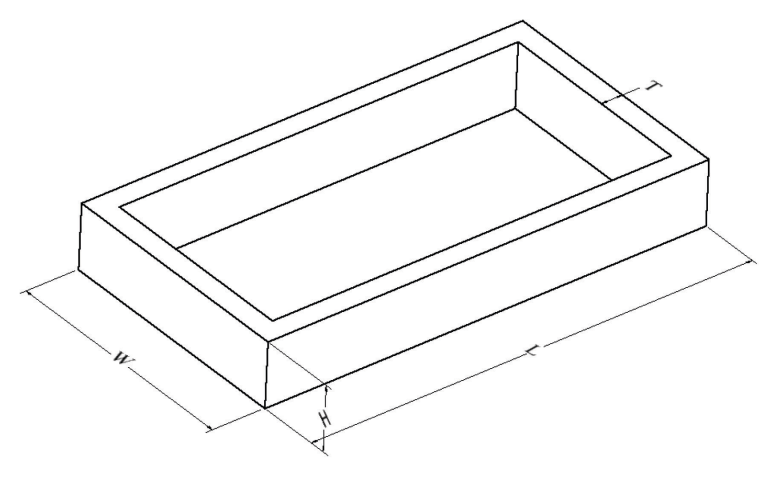


Fig. 13 Illustration of the geometry of the rectangular contour deposition

Table 4 Geometrical parameters of the LENS rectangular contour depositions

Number of layers	Length /mm	Width /mm	Thickness /mm	Height /mm
1	41.86	22.37	2.52	0.90
2	41.86	22.37	2.20	1.90
4	31.80	19.80	2.10	4.10
_ 5	41.86	22.37	2.72	4.43

Through detailed process simulation and modified inherent strain method, the maximum residual distortion in the vertical direction for the rectangular contours with different number of layers is listed in Table 5. The difference between the results obtained by the two different methods is very small, which indicates good accuracy for the proposed method. Although the substrate deformation results are much more consistent for layers 2 through 5 cases, we did not find an obvious trend in the substrate deformation results for the different number of deposition layers. Regarding a larger error in the one-layer case, a reasonable explanation is that it may not be so robust to identify the intermediate state of a long single layer deposition using exactly the same way established based on the multi-layer LENS process. Since the difference was acceptable when the same way of identifying the intermediate state was applied in all the cases, the one-layer contour case was still included to demonstrate the efficiency of the proposed method. In addition, the computational times of the detailed process simulation and the modified inherent strain method are shown in Table 5. The computational efficiency has a significant improvement (e.g. nearly 80x speedup for the 5-layer case) due to benefit of the proposed method.

Table 5 Maximum vertical residual distortion of the part with rectangular contour deposition and computational times by the detailed process simulation and the modified inherent strain method

Number –	Detailed pr	ocess simulation	Modified inl	- Distortion	
of layers	Distortion (mm)	Computational time (min)	Distortion (mm)	Computational time (min)	Error (%)
1	0.499	134.0	0.432	2.4	13.4
2	0.776	153.6	0.798	3.2	2.8
4	0.950	398.1	0.973	4.2	2.4
5	1.157	439.2	1.131	4.8	2.2

Meanwhile, the respective vertical displacement profiles of the rectangular contour wall with two layers and five layers obtained from the two different methods are shown in Figs. 14 and 15. As can be seen, the maximum residual distortion occurs at the free end of the substrate in the vertical direction. Clearly, the distribution of the vertical displacement field obtained in two ways is the same: A local region with negative vertical displacement exists close to the clamped end of the substrate, and positive deflections always occur along the free end. By comparison, very good agreement between the vertical displacement profiles can be clearly seen, which strongly verifies accuracy of the proposed modified inherent strain method for predicting residual distortion of the LENS process.

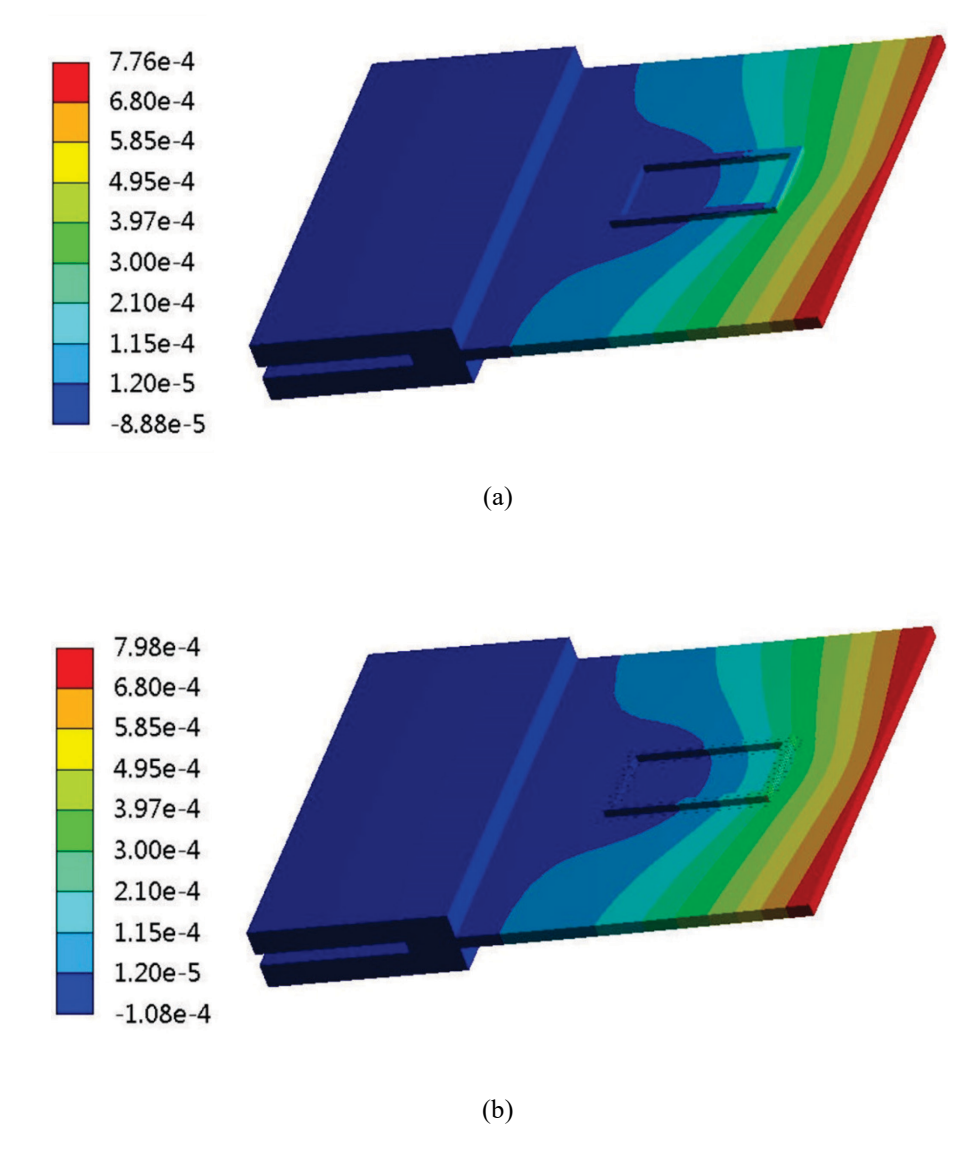


Fig. 14 Vertical residual distortion (unit: m) of the part with the two-layer contour deposition (a) by the detail process simulation (b) by the modified inherent strain method

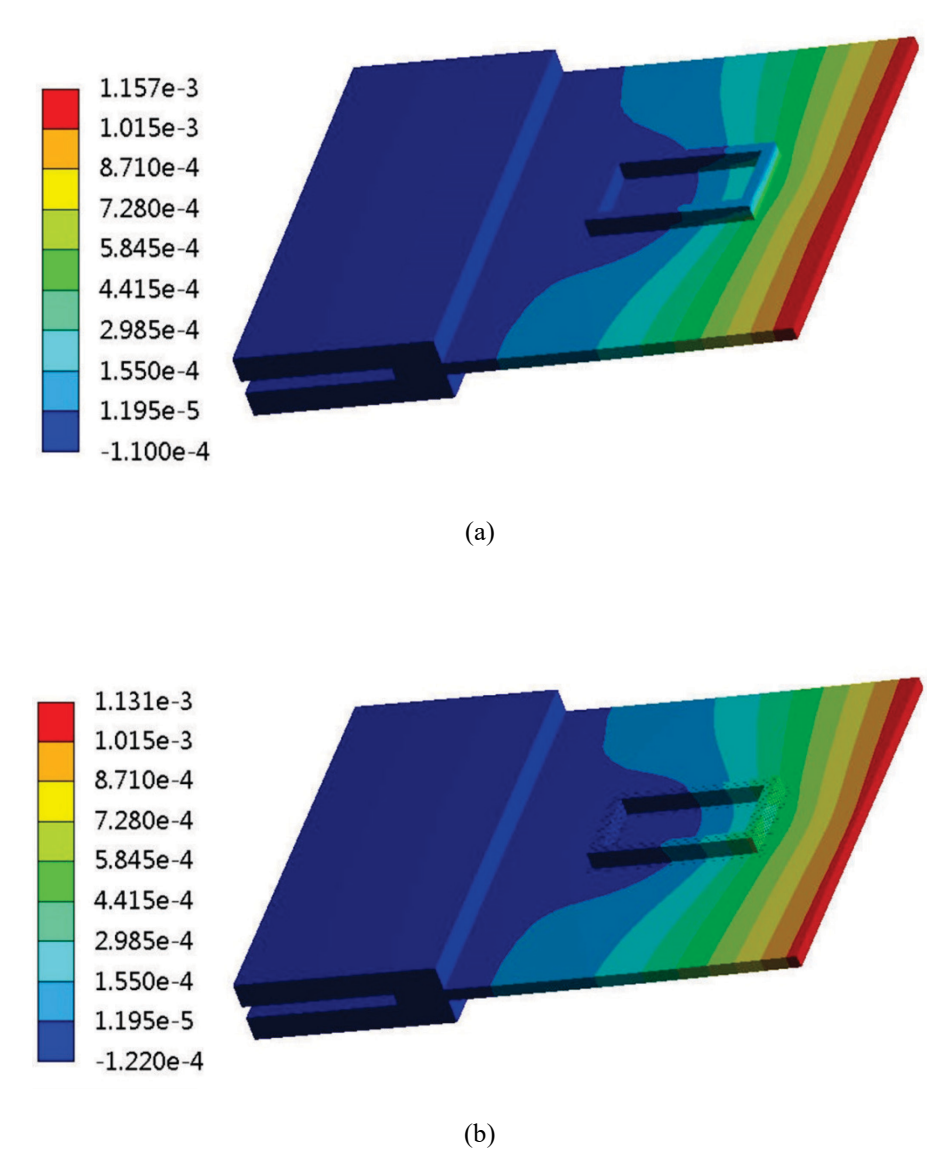


Fig. 15 Vertical residual distortion (unit: m) of the part with the five-layer contour deposition (a) by detailed process simulation (b) by the modified inherent strain method

Finally, to further validate the modified inherent strain theory, we conduct experiment to measure residual distortion resulting from the LENS process. A five-layer rectangular contour shown in Fig. 16 was manufactured using the LENS system. As mentioned in Sec. 3, residual distortion in the vertical direction is measured using a 3D laser scanning device. Surface profiles of the residual vertical distortion of the substrate obtained by three different methods, namely the modified inherent strain method, detailed process simulation, and the experimental measurement, are shown in Fig. 17. Clearly the distributions of the distortion field are very similar to each other. Note for the experimental result shown in Fig. 17(c), the flexural behavior is slightly stronger compared to the results obtained by the detailed process simulations and the modified inherent strain method. The possible reason is that there exists a little residual stress in the substrates since some machining treatment was done in the manufacturing process. The AM process may contribute to releasing the

residual stress in the substrate, generate some bending and affect the distribution of the AM-induced distortions. This explanation is acceptable since we had similar observations in other experiments using the same substrates.

In addition, both the minimum and maximum vertical residual distortions of the substrate are listed in Table 6. A concern is that the minimum distortion magnitudes are roughly 50 percent different from the experiment and two possible reasons are provided. First, the resolution of the laser scanning device is ±0.075mm, which may induce some error to the deformation measurement. As seen in the table, the magnitudes of the minimum distortion obtained by the detailed process simulation and the modified inherent strain method are very small and close to the measurement precision. The experimental measurement of the residual distortion may have some uncertainty caused by system errors, leading to slightly larger magnitudes (see Table 6). Second, the large error also has to do with the inaccurate boundary condition of the clamp since the minimum distortion location is close to the clamp. In the experiment, the fixtures were clamped by only several bolts as seen in Fig. 16. However, all the nodes of the fixtures were fixed strictly as the mechanical boundary conditions in our simulations. As a result, a relatively smaller distortion is seen in the simulation results, but generally, the maximum residual distortions are in excellent agreement with each other. From these results, the effectiveness and accuracy of the modified inherent strain method are both proved.

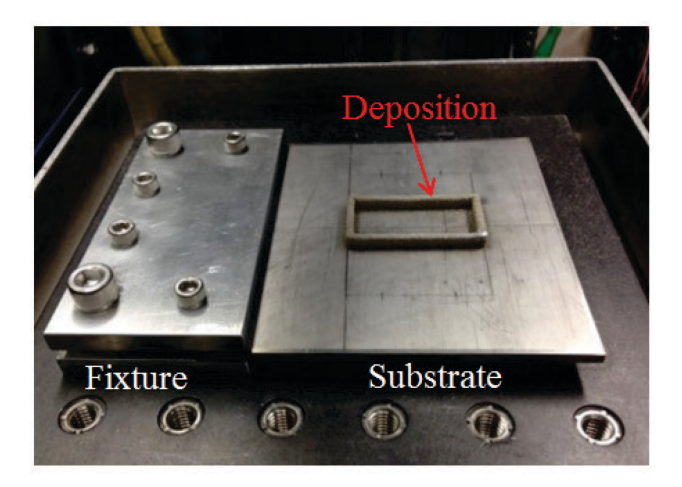


Fig. 16 Experimental setup for LENS and the five-layer contour deposition

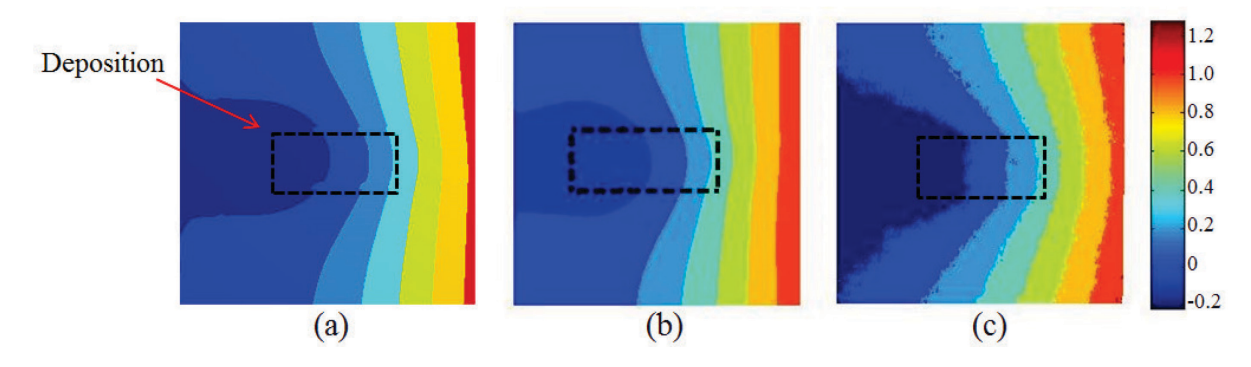


Fig. 17 Vertical residual distortion (unit: mm) of the substrate with LENS deposition of five-layer rectangular contour by (a) modified inherent strain method (b) detailed process simulation (c) experimental measurement

Table 6 Vertical residual distortion (unit: mm) of the substrate with a LENS deposited five-layer rectangular contour in three different ways

	Minimum	Maximum	Relative error of the maximum distortion (%)
Modified inherent strain method	-0.121	1.131	11.7
Detailed process simulation	-0.107	1.157	9.7
Experimental measurement	-0.217	1.281	

In this section, all the deposition lines were simulated and the inherent strains for the entire part were extracted and applied back to the LENS build. Compared to the thermomechanical simulation results, many features of the residual deformation can still be seen when this full-scale inherent strain approach is employed. This full-scale inherent strain approach is simply used to verify the accuracy of the modified model proposed in Eq. (6).

4.3 Single-walled depositions on a flat substrate fixed at bottom

The cantilever fixture is employed to hasten the residual distortion caused by the AM process so that the bottom surface of the substrate with the maximum residual distortion can be measured experimentally. However, many parts fabricated by the AM technology are built on a flat surface so that the residual distortion is minimized. The distortion of the parts in these cases will be much different from the parts investigated in our study, c.f. Refs. [27, 59]. Thus, in order to demonstrate that the proposed inherent strain model is also applicable to model those structures, deposition on a flat Ti64 substrate fixed at the bottom shown in Fig. 18 is employed in the following example. The size of the substrate is $102 \times 102 \times 6$ mm³. Regarding the thermal boundary, a constant temperature of 25 °C is applied to the bottom surface of the substrate and forced convection is applied to the rest of the surfaces. And the residual distortion of the 3-layer and 5-layer single-walled depositions will be investigated. The sizes of the two deposition models are identical to those shown in Sec. 4.1 (see Table 1). As shown in Fig. 18, the finite element mesh employed for the depositions remain the same with those in Sec. 4.1.

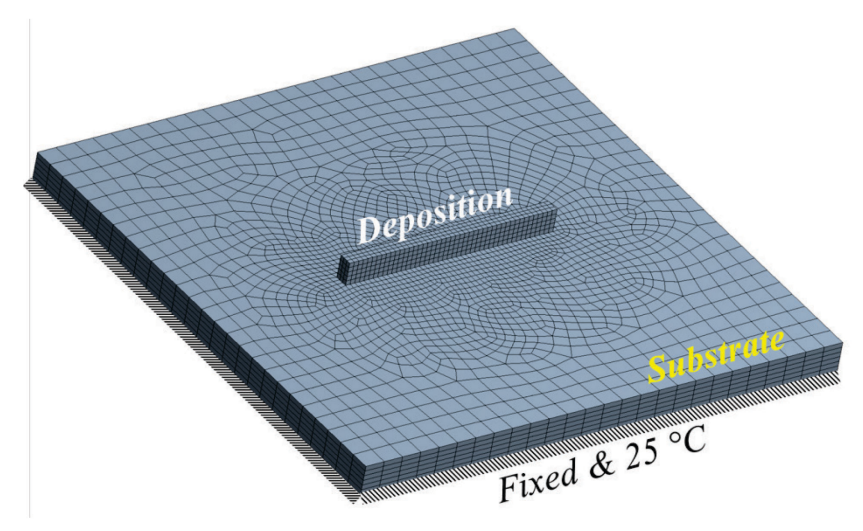


Fig. 18 Single-walled deposition model built on a flat substrate fixed at the bottom

Apart from the difference in the thermal and mechanical boundary conditions, the other involved parameters such as the laser power, scan velocity and laser absorption efficiency are the same as

in Sec. 4.1 in the full-scale process simulation. Based on the strain history of the process simulation, the intermediate and steady state are identified and the inherent strain values are extracted. The distribution of the elemental inherent strain values is similar as seen in Fig. 9. An interesting finding is that the obtained inherent strain values generally have a larger mean magnitude of (-0.013, -0.003, 0.012) compared with the cases in Sec. 4.1, which may indicate the influence of employing the bottom-fixed flat substrate as a stronger mechanical constraint. Through the same application method as in Sec. 4.1, the predicted residual distortion of the single-walled depositions by the modified inherent strain method can be obtained. For example, the comparison of the residual total deformation of the 5-layer deposition model by two different methods is shown in Fig. 19. The general deformed pattern of the deposition is similar, and the magnitudes of the global maximum total deformation are very close.

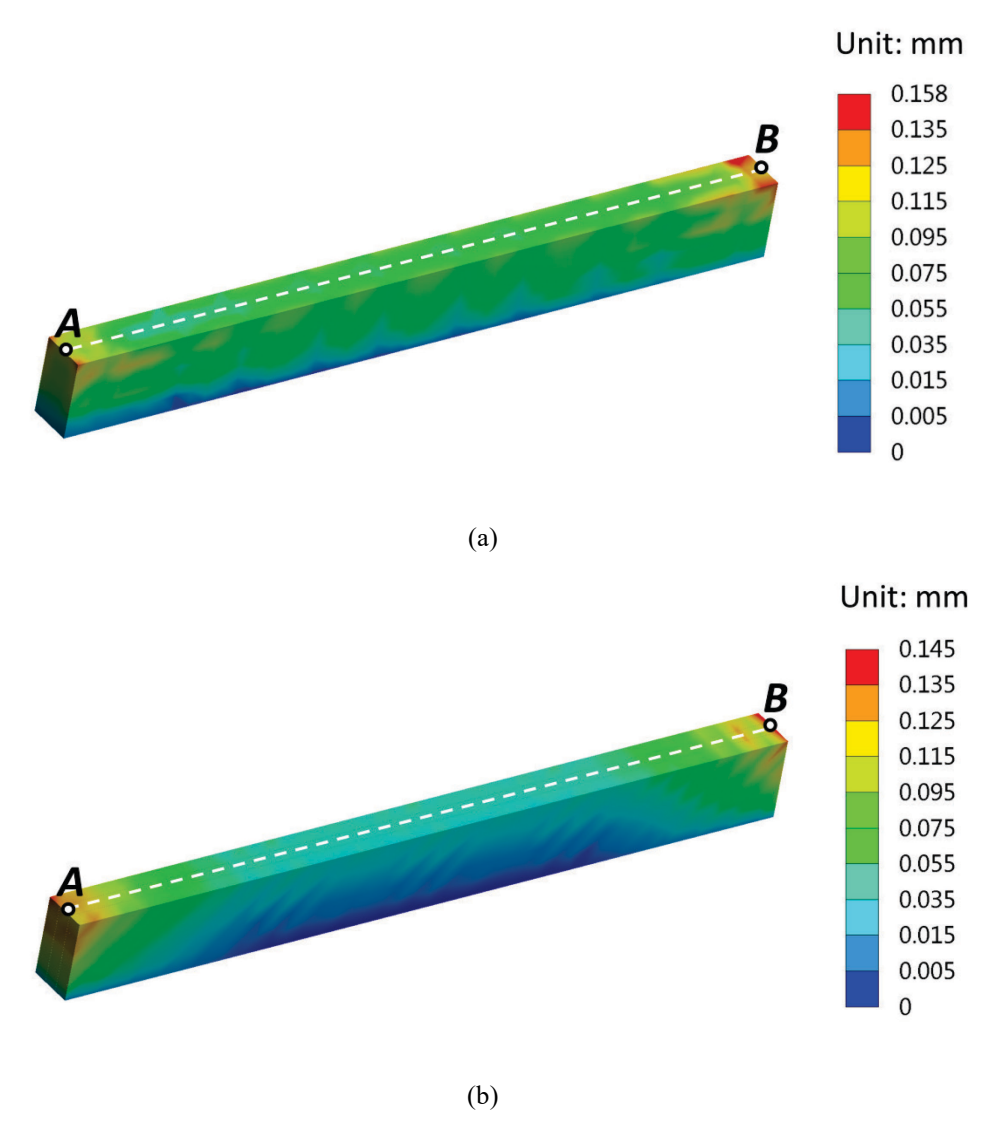


Fig. 19 Total residual deformation of the 5-layer single-walled deposition built on a bottom-fixed flat substrate obtained by (a) full-scale detailed process simulation, and (b) modified inherent strain method

For further comparison, the averaged total displacements at the two center points (A and B, see Fig. 19) on the two ends of the 3-layer and 5-layer deposition are tabulated in Table 7. Good agreement can be seen between the results obtained by the proposed inherent strain model and full-

scale detailed process simulation. Based on the results obtained from the two examples above, it can be concluded that the proposed model has general applicability to AM build scenarios with different boundary conditions.

1 abic / Residual total deformation (unit, min) of the single-wance depositions by two different inclined	Table 7 Residual total deformation	(unit: mm)	of the single-walled de	positions by ty	vo different methods
---	------------------------------------	------------	-------------------------	-----------------	----------------------

Nissals and G		Point A			Point B	
Number of layers	Full-scale detailed process simulation	Modified inherent strain method	Error (%)	Full-scale detailed process simulation	Modified inherent strain method	Error (%)
3	0.078	0.082	5.1	0.106	0.113	6.6
5	0.121	0.128	5.8	0.134	0.142	6.0

5. Mean inherent strain approach based on full-scale detailed simulation of line depositions

For single-walled structures containing many layers, in order to achieve satisfactory results, we propose that typical inherent strains extracted from two successive line deposition layers can ensure prediction accuracy. It is unreasonable to only simulate a one-layer line deposition model for extracting typical inherent strains because the re-melting process is not considered in this one-layer process model. On the other hand, in the LENS processing of the single-walled model, the deposited materials have enough time to cool down since the laser scanning speed is low (2 mm/s) and the length of the deposition line is large. Moreover, the large substrate is also made of the same Ti64 material with the deposition. Thus, it is not necessary to simulate more than two deposition lines to extract the inherent strains, since we can assume that most of the deposition lines experience the same melting and re-melting process.

To verify the above statement is correct, a representative volume of the full-scale two-layer and three-layer line deposition model is employed in the detailed process simulation to extract the inherent strains, respectively. As illustrated in Fig. 9, the inherent strains are averaged over the entire length of the deposition line. Hence a mean strain vector of (-0.0070, -0.002, 0.008) is obtained for the two-layer model, while (-0.0073, -0.003, 0.007) is obtained for the three-layer case. The inherent strain vector is converted to orthogonal CTEs and uniformly assigned to the multi-layer models as thermal material properties. In the solution, the elements of the multi-layer models are activated layer-by-layer and unit temperature is applied as the external load. The results for the three-layer and five-layer wall structures obtained by the layered inherent strain method and detailed process simulation are shown in Table 8. The errors are a little larger than the results obtained from full-scale detailed simulation of the entire build shown in Table 3. A possible reason is that the mean inherent strains, which are accurate only in the middle region of a large part, are applied uniformly to all the elements including those close to the surface. Despite the difference, very good agreement is shown between the results obtained from the two different methods. Our results demonstrate that only two deposition layers are needed in the representative volume model to ensure accuracy. However, if still higher accuracy is desired, three or more deposition layers may be employed to extract the inherent strains.

Table 8 Maximum vertical residual distortion of the substrate with LENS deposited three- and five-layer straight wall structure and computational times by detailed process simulation and layered inherent strain method

			Simulation based on mean inherent strain				
Number of layers	Detailed pr	rocess simulation	Extracted from two-layer model		Extracted from three-layer model		
	Distortion (mm)	Computational time (min)	Distortion (mm)	Computational time (min)	Distortion (mm)	Computational time (min)	
3	0.584	43.7	0.534	2.1	0.553	2.8	
5	0.937	57.6	1.024	2.5	1.063	3.2	

To verify that the proposed method is an efficient approach with low computational effort, comparison between the proposed method and detailed process simulation has been provided in terms of the computational effort required. Table 8 shows computational times for the straight five-layer single-walled deposition case in the full-scale detailed process simulation and the modified inherent strain method, respectively. Note that the proposed method allows the computational time to be reduced by ~20 times. Clearly, this comparison demonstrates the good computational efficiency of the proposed method.

6. Practical inherent strain method based on small-scale detailed simulation

6.1 Description of proposed method

Inspired by the assumption in Sec. 5 that nearly all the elements in a deposition line experience similar physical process, the entire length of a long deposition line does not need to be considered in the representative volume model. Therefore, for the LENS process concerned in this paper, we have investigated how to determine a reasonable small-scale model to extract the mean inherent strains for different single-walled structures. This section introduces details of the small-scale model with particular emphasis on the following three aspects:

(1) Determination of the small-scale model

The geometry of the small-scale model for the LENS process should be a two-layer line deposition model. It is also reasonable to use a three-layer deposition model if the computational cost can be afforded. However, the benefit of utilizing a three-layer deposition as the small-scale model is little, as the mean inherent strains extracted from the two-layer and three-layer single-walled model are very close to each other (see Sec. 5).

The size of the two-layer small-scale model depends on the specific DED process parameters including laser power, scanning speed and powder feed rate. For the process parameters employed for LENS processing of Ti64 in this work (laser power 300W, scanning speed 2mm/s and powder feed rate 6~8 rpm), the size of the small-scale two-layer model can be defined as $20 \times 2.0 \times 1.8$ mm³ as shown in Fig. 20(a). Note the length for the small-scale process model should be selected to ensure that the temperature along the scan line in the simulation reaches steady state. (The inherent strains will then be extracted from the steady state region as steady state behavior is dominant in most structures of interest.) The heat source should move far away from the starting end to ensure that the temperature contour maintains a stable shape with a comet-like tail over the layer (see Fig. 20(b), for example). The mesh dimension of the two-layer small-scale model is shown in Fig. 20(a). As a common practice [26, 27, 34], one element through the thickness is employed to model

one single layer. For the element mesh along the laser scanning direction, given the laser beam diameter (~0.6 mm) of the LENS machine, the layer is meshed with 40×3 elements in the length and width dimension (see Fig. 20(a)). Employing the element birth and death method, 50 load steps are used to simulate the deposition process of one single layer.

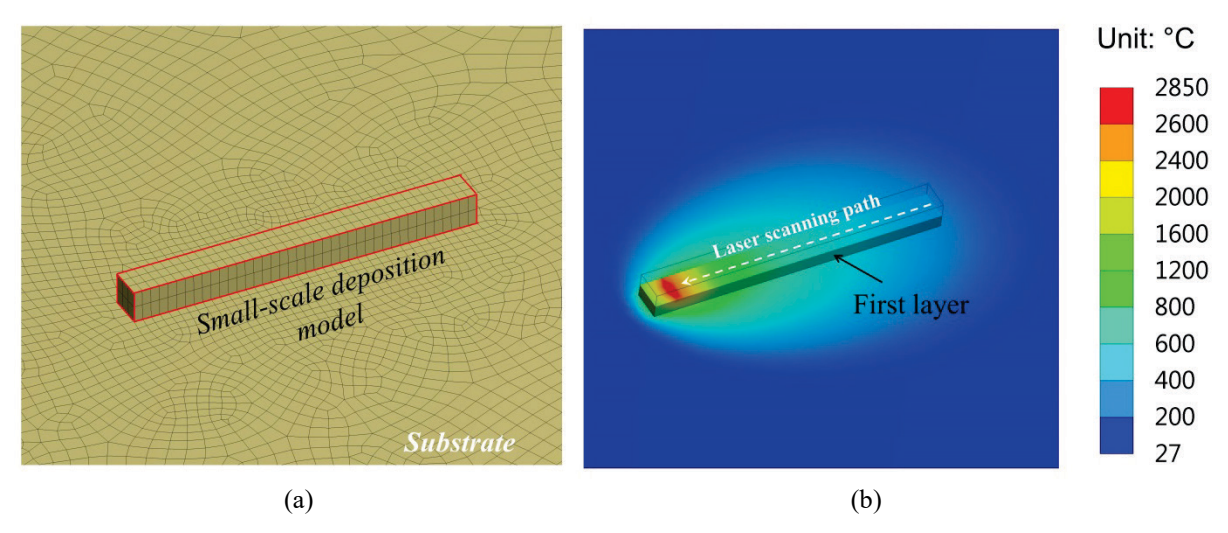


Fig. 20 Typical features of the small-scale model: (a) geometry and mesh model and (b) stabilized temperature contour in a deposition layer

(2) Evaluation of mean inherent strain

After the small-scale simulation is finished, the elastic and plastic strain history of any material point in the deposition can be recorded conveniently using APDL commands. Material points in the centerline of bottom layer in the small-scale model are selected as the sampling points to compute the mean inherent strain. The elastic and plastic strains in the intermediate and steady states of the selected sampling points are obtained from the small-scale simulation results. Then the inherent strains at each sampling point can be computed based on the modified inherent strain definition given in Eq. (6). For the strain component parallel to the laser scanning direction, the inherent strains are summed up and averaged over the entire layer dimension to obtain the mean inherent strain components. Similarly, the same procedure is carried out for the remaining two inherent strain components perpendicular to the laser scanning path and in the build direction. In this manner, the three normal components of the mean inherent strain vector can be evaluated. In this section, the mean inherent strain vector based on the small-scale model is determined to be (-0.0069, -0.002, 0.008) and will be applied to the rectangular contour deposition model to verify its accuracy.

(3) Application to a different single-walled structure

These normal inherent strains are averaged into an inherent strain vector as discussed above. To implement this conveniently in commercial finite element software, the mean inherent strain vector is treated as orthotropic CTEs for the large model. The rectangular contour wall deposition model is considered as a different part to illustrate the application of the mean inherent strain extracted from the small-scale detailed simulation model. Note that the in-layer components of the mean inherent strain vector correspond to the directions parallel and perpendicular to the laser scanning direction. However, since the laser scanning changes direction on different sides of the rectangular

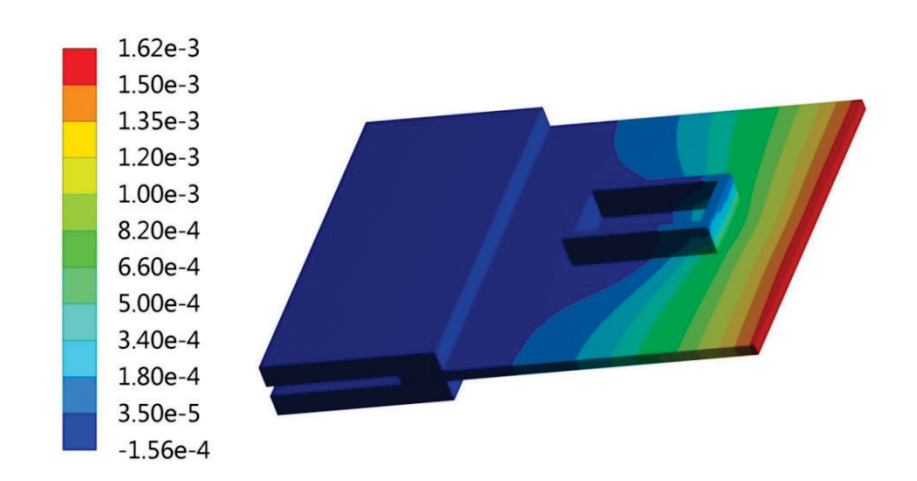
contour deposition model and forms a closed contour path, a reasonable way is to apply the averaged magnitude for the in-layer components of the mean inherent strain vector to the layers containing different laser scanning paths. Therefore, the mean inherent strain vector for each layer of the rectangular contour becomes (-0.0045, -0.0045, 0.008) after averaging and is then applied uniformly to each layer of the rectangular contour wall model. The layers in the large model are activated layer-by-layer, and a unit temperature increase is applied to the newly activated layer to introduce the inherent strains as initial strains. Generally, the mean inherent strain obtained through the small-scale simulation can be applied to different single-walled structures and predict residual deformation efficiently.

6.2 Results and discussion

The predicted maximum vertical deformation of the five-layer and ten-layer rectangular deposition model using the new mean inherent strain vector is shown in Table 9 together with results obtained from full-scale detailed process simulation. In addition, the vertical residual deformation profile of the ten-layer rectangular contour deposition model is shown in Fig. 21. Clearly, compared with those full-scale simulation results, good agreement can be observed, and the modified inherent strain method based on the small-scale simulation is successfully validated when applied to a different model. Nonetheless, a possible explanation for the relatively large error in the ten-layer case is that, during deposition of large parts, the workpiece experiences different thermal energy transfer. As a result, the re-melting zone changes during the deposition process, and it is normally larger with increasing distance from the substrate. This phenomenon could affect the extracted inherent strains, and it may be inappropriate to use the same mean inherent strain vector for all the layers in a large AM build. The detailed relationship of the inherent strains and the thermal lifecycle in the deposition process requires more investigation in future.

Table 9 Maximum vertical deformation of the rectangular contour deposition model using full-scale process simulation and the modified inherent strain method based on small-scale process simulation

C	Maximum vertical deformation (mm)				
Cases	Full-scale process simulation	Modified inherent strain method	Error (%)		
5-layer	1.157	1.181	2.1		
10-layer	1.622	1.780	9.7		



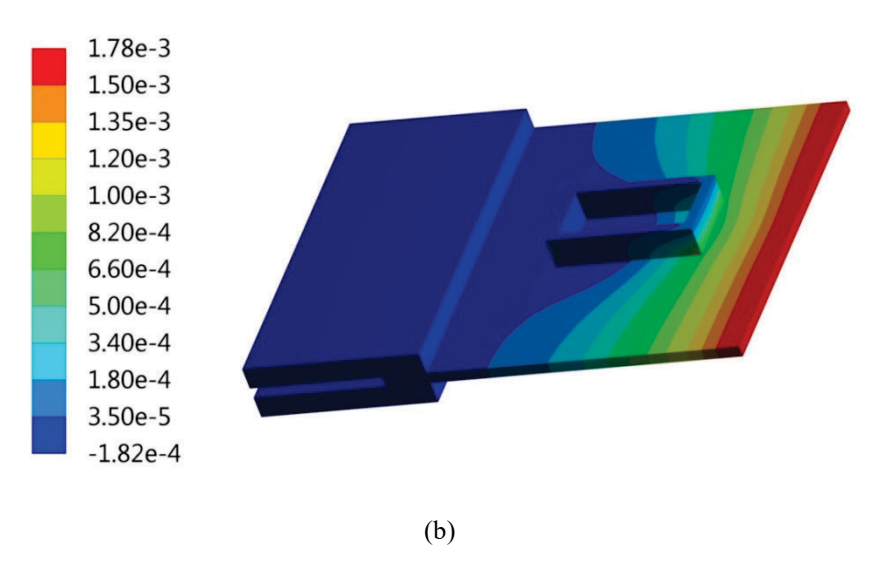


Fig. 21 the predicted distribution of vertical residual deformation (unit: m) of the ten-layer rectangular contour deposition model by (a) full-scale process simulation (b) mean inherent strain vector method

Regarding efficiency of the proposed method, the computational times of the two new cases of the five-layer and ten-layer rectangular contour deposition models are shown in Table 10. The time needed for the small-scale simulation model (33.8 mins) has been added to the total computational time for the modified inherent stain method since it also takes time to evaluate the mean inherent strain vector. As shown in the table, even with the small-scale simulation time included, the modified inherent strain method is still much more efficient (10~15x speedup) than the full-scale detailed thermomechanical simulation. And if we consider only the time it takes to execute the modified inherent strain method, the improvement of the computational efficiency can be nearly 80 times.

Table 10 Comparison of detailed process simulation and the modified inherent strain method in terms of computational efforts required for the five-layer and ten-layer rectangular contour deposition model

	(Computational time (min)				
Cases	Evil socia detailed musesses	Modified inherent strain method				
	Full-scale detailed process - simulation	Including small-scale simulation	Excluding small-scale simulation			
5-layer	439.2	38.4	4.6			
10-layer	610.2	42.2	8.4			

Additionally, the same mesh is used when we apply the obtained inherent strains back to the deposition models in this paper. The benefit of doing this is that the inherent strains can be applied in a convenient element-by-element manner. If the mesh size of the detailed simulation model is different from that used for the estimation of the residual distortions, the calculated inherent strains

could be mapped to the model as a function of the location of the elements. For the model used for the detailed process simulation, the locations of those elements in the HAZ can be normalized to a standard range as seen in Fig. 9. Then for the model with a different mesh used for the prediction of the residual distortions, as for any element in the HAZ, according to its normalized location, the amount of the inherent strains to be assigned to the element can be calculated by interpolation using the normalized curves.

7. Conclusions

Prediction of residual distortion in a part built by an AM process has been inaccurate and time-consuming. In this paper, the modified inherent strain method is proposed for fast prediction of residual distortion of single-walled structures produced by a representative DED process in LENS. Specifically, a modified model is proposed to estimate the inherent strains from detailed process simulation, which are then applied to the part model to perform a layer-by-layer static analysis to simulate residual distortion. To validate the proposed model, the inherent strains obtained from full-scale detailed simulation of the entire structure under consideration are applied back to the structure to predict residual distortion by static equilibrium analysis. The structures employed to validate the model include a single wall and rectangular contour wall by the LENS process. The accuracy and efficiency of the proposed method has been demonstrated by both numerical examples and experiments. It is also shown that the proposed model has general applicability to AM build scenarios with different boundary conditions.

As a first step to make the proposed method practical, the mean inherent strain concept is then proposed and extracted based on full-scale two-layer and three-layer line deposition models. Numerical examples have demonstrated that the mean inherent strain can be applied to single-walled structures having more layers to accurately predict the residual deformation much faster. Then to make the method truly practical, a small-scale detailed simulation model is proposed to extract the mean inherent strains, which are then applied to different single-walled structures for fast residual deformation prediction. Simulation results show that the modified inherent strain method is quite efficient, while the residual distortion of AM parts can be accurately computed within a short time.

As shown in Secs. 5 and 6, the assumption that most of the deposition lines experiences the same melting and re-melting process in the AM process may not be true in some cases. When the scan speed is high and the part is large, the workpiece may experience different thermal energy transfer due to the boundary effects of the substrate and the previous deposition layers with high temperature. In other words, the sampling positions of the small-scale model from the large part may also have some effects on the extracted inherent strains. To tackle this problem, further research is needed to investigate the temperature gradient in the deposition by performing many more detailed process simulations and experiments.

As pointed out, the modified inherent strain model is proposed based on single line depositions on top of each other, and hence validity of the model has been demonstrated only on single-walled structures in this work. The proposed model will need to be extended in order to treat more complex geometries consisting of scan lines not only on top of each other but also next to each other. For a large AM build, clearly it is impossible to simulate all the lines and layers before extracting the overall inherent strains. In addition, usually complex geometries may be deposited using complex laser scanning patterns in the AM process including DED and PBF. The influence

on the inherent strains by the process parameters such as the laser scanning path needs to be considered further. Thus the detailed depositing path needs be modeled in the simulation of a local region of the large part. This also means that simulating only a straight deposition line is not sufficient for computing the inherent strains accurately for complex geometries. Rather, a small section may be used as the representative volume to obtain the inherent strains necessary to simulate deformation of a large complex part efficiently. In addition to extending the proposed inherent strain model, further research is needed to investigate this approach and the associated accuracy and efficiency.

Acknowledgements

Financial support from National Science Foundation (CMMI-1634261) and Swanson School of Engineering at University of Pittsburgh is gratefully acknowledged. The authors wish to thank the anonymous reviewers for all the constructive comments during the review process.

Reference

- [1] P. Zhang, J. Toman, Y. Yu, E. Biyikli, M. Kirca, M. Chmielus, A.C. To, Efficient Design-Optimization of Variable-Density Hexagonal Cellular Structure by Additive Manufacturing: Theory and Validation, Journal of Manufacturing Science and Engineering 137(2) (2015) 021004.
- [2] L. Cheng, P. Zhang, E. Biyikli, J. Bai, J. Robbins, A. To, Efficient design optimization of variable-density cellular structures for additive manufacturing: theory and experimental validation, Rapid Prototyping Journal 23(4) (2017) 660-677.
- [3] J. Ding, P. Colegrove, J. Mehnen, S. Williams, F. Wang, P.S. Almeida, A computationally efficient finite element model of wire and arc additive manufacture, The International Journal of Advanced Manufacturing Technology 70(1-4) (2014) 227-236.
- [4] I. Gibson, D.W. Rosen, B. Stucker, Additive Manufacturing Technologies: Rapid Prototyping to Direct Digital Manufacturing, Springer, 2009.
- [5] J.P. Kruth, M. Leu, T. Nakagawa, Progress in additive manufacturing and rapid prototyping, CIRP Annals-Manufacturing Technology 47(2) (1998) 525-540.
- [6] L. Murr, S. Gaytan, F. Medina, H. Lopez, E. Martinez, B. Machado, D. Hernandez, L. Martinez, M. Lopez, R. Wicker, Next-generation biomedical implants using additive manufacturing of complex, cellular and functional mesh arrays, Philosophical Transactions of the Royal Society of London A: Mathematical, Physical and Engineering Sciences 368(1917) (2010) 1999-2032.
- [7] R. Hague, I. Campbell, P. Dickens, Implications on design of rapid manufacturing, Proceedings of the Institution of Mechanical Engineers, Part C: Journal of Mechanical Engineering Science 217(1) (2003) 25-30.
- [8] N. Hopkinson, R. Hague, P. Dickens, Rapid manufacturing: an industrial revolution for the digital age, John Wiley & Sons, 2006.
- [9] E.C. Santos, M. Shiomi, K. Osakada, T. Laoui, Rapid manufacturing of metal components by laser forming, International Journal of Machine Tools and Manufacture 46(12) (2006) 1459-1468.
- [10] P. Zhang, J. Liu, A.C. To, Role of anisotropic properties on topology optimization of additive manufactured load bearing structures, Scripta Materialia 135 (2017) 148-152.
- [11] M.P. Bendsoe, O. Sigmund, Topology optimization: theory, methods, and applications, Springer Science & Business Media, 2013.
- [12] O. Sigmund, K. Maute, Topology optimization approaches, Structural and Multidisciplinary Optimization 48(6) (2013) 1031-1055.
- [13] M.Y. Wang, X. Wang, D. Guo, A level set method for structural topology optimization, Computer Methods in Applied Mechanics and Engineering 192(1–2) (2003) 227-246.
- [14] G. Allaire, F. Jouve, A.-M. Toader, Structural optimization using sensitivity analysis and a level-set method, Journal of Computational Physics 194(1) (2004) 363-393.
- [15] J. Liu, A. Gaynor, S. Chen, Z. Kang, K. Suresh, A. Takezawa, L. Li, J. Kato, J. Tang, C. Wang, L. Cheng, X. Liang, A. To, Current and future trends in topology optimization for additive manufacturing, Structural and Multidisciplinary Optimization (2018) DOI: 10.1007/s00158-018-1994-3.
- [16] B. Baufeld, O. Van der Biest, R. Gault, Additive manufacturing of Ti–6Al–4V components by shaped metal deposition: microstructure and mechanical properties, Materials & Design 31 (2010) S106-S111.
- [17] I. Palčič, M. Balažic, M. Milfelner, B. Buchmeister, Potential of laser engineered net shaping (LENS) technology, Materials and Manufacturing Processes 24(7-8) (2009) 750-753.
- [18] R.P. Mudge, N.R. Wald, Laser engineered net shaping advances additive manufacturing and repair, Welding Journal-New York- 86(1) (2007) 44.

- [19] L. Li, Repair of directionally solidified superalloy GTD-111 by laser-engineered net shaping, Journal of materials science 41(23) (2006) 7886-7893.
- [20] H. Koehler, K. Partes, T. Seefeld, F. Vollertsen, Influence of laser reconditioning on fatigue properties of crankshafts, Physics Procedia 12 (2011) 512-518.
- [21] L. Van Belle, G. Vansteenkiste, J.C. Boyer, Investigation of residual stresses induced during the selective laser melting process, Key Engineering Materials, Trans Tech Publ, 2013, pp. 1828-1834.
- [22] F. Neugebauer, N. Keller, V. Ploshikhin, F. Feuerhahn, H. Koehler, Multi Scale FEM Simulation for Distortion Calculation in Additive Manufacturing of Hardening Stainless Steel, International Workshop on Thermal Forming an Welding Distortion, IWOTE 14, 2014.
- [23] D. Radaj, Heat effects of welding: temperature field, residual stress, distortion, Springer Science & Business Media, 2012.
- [24] W.E. Frazier, Metal additive manufacturing: a review, Journal of Materials Engineering and Performance 23(6) (2014) 1917-1928.
- [25] B. Schoinochoritis, D. Chantzis, K. Salonitis, Simulation of metallic powder bed additive manufacturing processes with the finite element method: A critical review, Proceedings of the Institution of Mechanical Engineers, Part B: Journal of Engineering Manufacture 231(1) (2017) 96-117.
- [26] B. Cheng, S. Shrestha, K. Chou, Stress and deformation evaluations of scanning strategy effect in selective laser melting, Additive Manufacturing 12 (2016) 240-251.
- [27] T. Mukherjee, W. Zhang, T. DebRoy, An improved prediction of residual stresses and distortion in additive manufacturing, Computational Materials Science 126 (2017) 360-372.
- [28] G. Vastola, G. Zhang, Q. Pei, Y.-W. Zhang, Controlling of residual stress in additive manufacturing of Ti6Al4V by finite element modeling, Additive Manufacturing 12 (2016) 231-239.
- [29] J. Heigel, P. Michaleris, E. Reutzel, Thermo-mechanical model development and validation of directed energy deposition additive manufacturing of Ti–6Al–4V, Additive manufacturing 5 (2015) 9-19.
- [30] M.F. Gouge, J.C. Heigel, P. Michaleris, T.A. Palmer, Modeling forced convection in the thermal simulation of laser cladding processes, The International Journal of Advanced Manufacturing Technology 79(1-4) (2015) 307-320.
- [31] Y. Zhang, J. Zhang, Finite element simulation and experimental validation of distortion and cracking failure phenomena in direct metal laser sintering fabricated component, Additive Manufacturing 16 (2017) 49-57.
- [32] E.R. Denlinger, J.C. Heigel, P. Michaleris, Residual stress and distortion modeling of electron beam direct manufacturing Ti-6Al-4V, Proceedings of the Institution of Mechanical Engineers, Part B: Journal of Engineering Manufacture 229(10) (2015) 1803-1813.
- [33] R. Moat, A. Pinkerton, L. Li, P. Withers, M. Preuss, Residual stresses in laser direct metal deposited Waspaloy, Materials Science and Engineering: A 528(6) (2011) 2288-2298.
- [34] P. Michaleris, Modeling metal deposition in heat transfer analyses of additive manufacturing processes, Finite Elements in Analysis and Design 86 (2014) 51-60.
- [35] E.R. Denlinger, J. Irwin, P. Michaleris, Thermomechanical modeling of additive manufacturing large parts, Journal of Manufacturing Science and Engineering 136(6) (2014) 061007.

- [36] Y. Ueda, K. Fukuda, M. Tanigawa, New measuring method of three dimensional residual stresses based on theory of inherent strain (welding mechanics, strength & design), Transactions of JWRI 8(2) (1979) 249-256.
- [37] M.R. Hill, D.V. Nelson, The inherent strain method for residual stress determination and its application to a long welded joint, ASME-PUBLICATIONS-PVP 318 (1995) 343-352.
- [38] M. Yuan, Y. Ueda, Prediction of residual stresses in welded T-and I-joints using inherent strains, Journal of engineering materials and technology 118(2) (1996) 229-234.
- [39] D. Deng, H. Murakawa, W. Liang, Numerical simulation of welding distortion in large structures, Computer methods in applied mechanics and engineering 196(45) (2007) 4613-4627.
- [40] H. Murakawa, D. Deng, N. Ma, J. Wang, Applications of inherent strain and interface element to simulation of welding deformation in thin plate structures, Computational Materials Science 51(1) (2012) 43-52.
- [41] L. Zhang, P. Michaleris, P. Marugabandhu, Evaluation of applied plastic strain methods for welding distortion prediction, Journal of Manufacturing Science and Engineering 129(6) (2007) 1000-1010.
- [42] P. Michaleris, L. Zhang, S. Bhide, P. Marugabandhu, Evaluation of 2D, 3D and applied plastic strain methods for predicting buckling welding distortion and residual stress, Science and Technology of Welding & Joining (2013).
- [43] Y.-X. Wang, P. Zhang, Z.-G. Hou, C.-Z. Li, Inherent strain method and thermal elastic-plastic analysis of welding deformation of a thin-wall beam, Journal of Mechanics 24(04) (2008) 301-309.
- [44] N. Keller, V. Ploshikhin, New method for fast predictions of residual stress and distortion of AM parts, Proceedings of Solid Freeform Fabrication (SFF) Conference, 2014.
- [45] G. Huang, P. Mehmert, H. Schafstall, A. Buijk, On The Creation of a New Finite Element Simulation Environment for Additive Manufacturing, NAFEMS Americas Conference, Session Reviews, Session 7/1D, 2016.
- [46] N. Keller, J. Schlasche, C. Kober, V. Ploshikhin, C. Werner, T. Domagala, Distortion Compensation in Laser Beam Melting Processes, MSTAM 2014 Proceedings of the 1st International Symposium Materials Science and Technology of Additive Manufacturing, 2015.
- [47] S. Afazov, W.A. Denmark, B.L. Toralles, A. Holloway, A. Yaghi, Distortion Prediction and Compensation in Selective Laser Melting, Additive Manufacturing 17 (2017) 15-22.
- [48] Y. Ueda, H. Murakawa, N. Ma, Welding deformation and residual stress prevention, Elsevier2012.
- [49] A. Anca, V.D. Fachinotti, G. Escobar Palafox, A. Cardona, Computational modelling of shaped metal deposition, International journal for numerical methods in engineering 85(1) (2011) 84-106.
- [50] V. Fallah, M. Alimardani, S.F. Corbin, A. Khajepour, Temporal development of melt-pool morphology and clad geometry in laser powder deposition, Computational materials science 50(7) (2011) 2124-2134.
- [51] X. Liang, Q. Chen, L. Cheng, A. To, A Modified Inherent Strain Method for Fast Prediction of Residual Deformation in Additive Manufacturing of Metal Parts, Proceedings of Solid Freeform Fabrication (SFF) Conference, 2017.
- [52] S. Marimuthu, D. Clark, J. Allen, A. Kamara, P. Mativenga, L. Li, R. Scudamore, Finite element modelling of substrate thermal distortion in direct laser additive manufacture of an aeroengine component, Proceedings of the Institution of Mechanical Engineers, Part C: Journal of Mechanical Engineering Science 227(9) (2013) 1987-1999.

- [53] R. Ye, J.E. Smugeresky, B. Zheng, Y. Zhou, E.J. Lavernia, Numerical modeling of the thermal behavior during the LENS® process, Materials Science and Engineering: A 428(1) (2006) 47-53. [54] L. Wang, S. Felicelli, Y. Gooroochurn, P. Wang, M. Horstemeyer, Optimization of the LENS® process for steady molten pool size, Materials Science and Engineering: A 474(1) (2008) 148-156.
- [55] J. Goldak, A. Chakravarti, M. Bibby, A new finite element model for welding heat sources, Metallurgical transactions B 15(2) (1984) 299-305.
- [56] Q. Yang, P. Zhang, L. Cheng, Z. Min, M. Chyu, A.C. To, Finite element modeling and validation of thermomechanical behavior of Ti-6Al-4V in directed energy deposition additive manufacturing, Additive Manufacturing 12 (2016) 169-177.
- [57] S. Joshi, J. Hildebrand, A.S. Aloraier, T. Rabczuk, Characterization of material properties and heat source parameters in welding simulation of two overlapping beads on a substrate plate, Computational Materials Science 69 (2013) 559-565.
- [58] M. Chiumenti, M. Cervera, A. Salmi, C.A. De Saracibar, N. Dialami, K. Matsui, Finite element modeling of multi-pass welding and shaped metal deposition processes, Computer methods in applied mechanics and engineering 199(37) (2010) 2343-2359.
- [59] H. Peng, D.B. Go, R. Billo, S. Gong, M.R. Shankar, B.A. Gatrell, J. Budzinski, P. Ostiguy, R. Attardo, C. Tomonto, Part-scale model for fast prediction of thermal distortion in DMLS additive manufacturing; Part 2: a quasi-static thermo-mechanical model, Proceedings of Solid Freeform Fabrication (SFF) Conference (2016).